Thermodynamic stability of droplets, bubbles and thick films in open and closed pores

Magnus Aa. Gjennestad[a,*], Øivind Wilhelmsen[b,c]

[a] *PoreLab/Department of Physics, Norwegian University of Science and Technology, Høgskoleringen 5, NO-7491 Trondheim, Norway*
[b] *Department of Energy and Process Engineering, Norwegian University of Science and Technology, Kolbjørn Hejes vei 1B, NO-7491 Trondheim, Norway*
[c] *PoreLab/SINTEF Energy Research, Sem Sælands vei 11, NO-7034 Trondheim, Norway*

Abstract

A fluid in a pore can form diverse heterogeneous structures. We combine a capillary description with the cubic-plus-association equation of state to study the thermodynamic stability of droplets, bubbles and films of water at 358 K in a cylindrically symmetric pore. The equilibrium structure depends strongly on the size of the pore and whether the pore is closed (canonical ensemble) or connected to a particle reservoir (grand canonical ensemble). A new methodology is presented to analyze the thermodynamic stability of films, where the integral that describes the total energy of the system is approximated by a quadrature rule. We show that, for large pores, the thermodynamic stability limit of adsorbed droplets and bubbles in both open and closed pores is governed by their mechanical stability, which is closely linked to the pore shape. This is also the case for a film in a closed pore. In open pores, the film is chemically unstable except for very low film-phase contact angles and for a limited range in external pressure. This result emphasizes the need to invoke a complete thermodynamic stability analysis, and not restrict the discussion to mechanical stability. A common feature for most of the heterogeneous structures examined is the appearance of regions where the structure is metastable with respect to a pore filled with a homogeneous fluid. In the closed pores, these regions grow considerably in size when the pores become smaller. This can be understood from the larger energy cost of the interfaces relative to the energy gained from having two phases. Complete phase diagrams are presented that compare all the investigated structures. In open pores at equilibrium, the most stable structure is either the homogeneous phase or adsorbed droplets and bubbles, depending on the type of phase in the external reservoir. Smaller pores allow for droplets and bubbles to adsorb for a larger span in pressure. In closed pores, most of the investigated configurations can occur depending on the total density, the contact angle and the pore shape. The analysis presented in this work is a step towards developing a thermodynamic framework to map the rich heterogeneous phase diagram of porous media and other confined systems.

Keywords: thermodynamics, stability, droplet, bubble, film, pore

1. Introduction

Some phenomena occur exclusively in pores or under strong confinement. In porous materials, a liquid phase can form at pressures below the saturation pressure during capillary condensation [1–4], liquid water can be stretched to negative pressures exceeding 140 MPa in quartz inclusions [5, 6] and giant charge reversal has been observed in confined systems filled with electrolytes [7]. The understanding of such systems is at the core of widely different topics such as porous media science [8], atmospheric science [9] and biology [10].

While the thermodynamics of homogeneous systems is well understood [11], this is not the case for heterogeneous systems, as evident e.g. from the large deviations between experiments, theory and simulations for the formation of drops [12, 13]. Both in bulk systems and in systems under confinement, equilibrium is characterized by a minimum of an energy state function whose nature is determined by the boundary conditions. For instance, in a closed container at constant temperature, equilibrium is a minimum of the Helmholtz energy, while the Gibbs energy is minimum at atmospheric conditions [11]

A complicating factor in pores, is that multiple heterogeneous structures such as films, adsorbed or free droplets and bubbles, and combinations of these, could all be stationary states of the same energy state function [14]. Such states are typically characterized by uniform temperature, equality of chemical potentials and mechanical equilibrium [11, 15]. These conditions being satisfied however, does not imply a minimum, as the stationary state can also be a maximum or a saddle point [16]. To determine the equilibrium state, it is necessary to employ thermodynamic stability analysis [17], where the outcome depends strongly on the boundary conditions. For instance, bubbles and droplets are known to be unstable at atmospheric conditions, as they represent saddle points in the Gibbs energy landscape [16]. However, in confined systems, bubbles and droplets can be minima in the Helmholtz energy and thus be stable [18, 19].

In the literature on the stability of heterogeneous structures, many works have studied *thin* films, often in combination with adsorbed droplets [20–22]. Films are characterized as either

*Corresponding author.
Email addresses: magnus.aa.gjennestad@ntnu.no (Magnus Aa. Gjennestad), magnus@aashammer.net (Magnus Aa. Gjennestad)

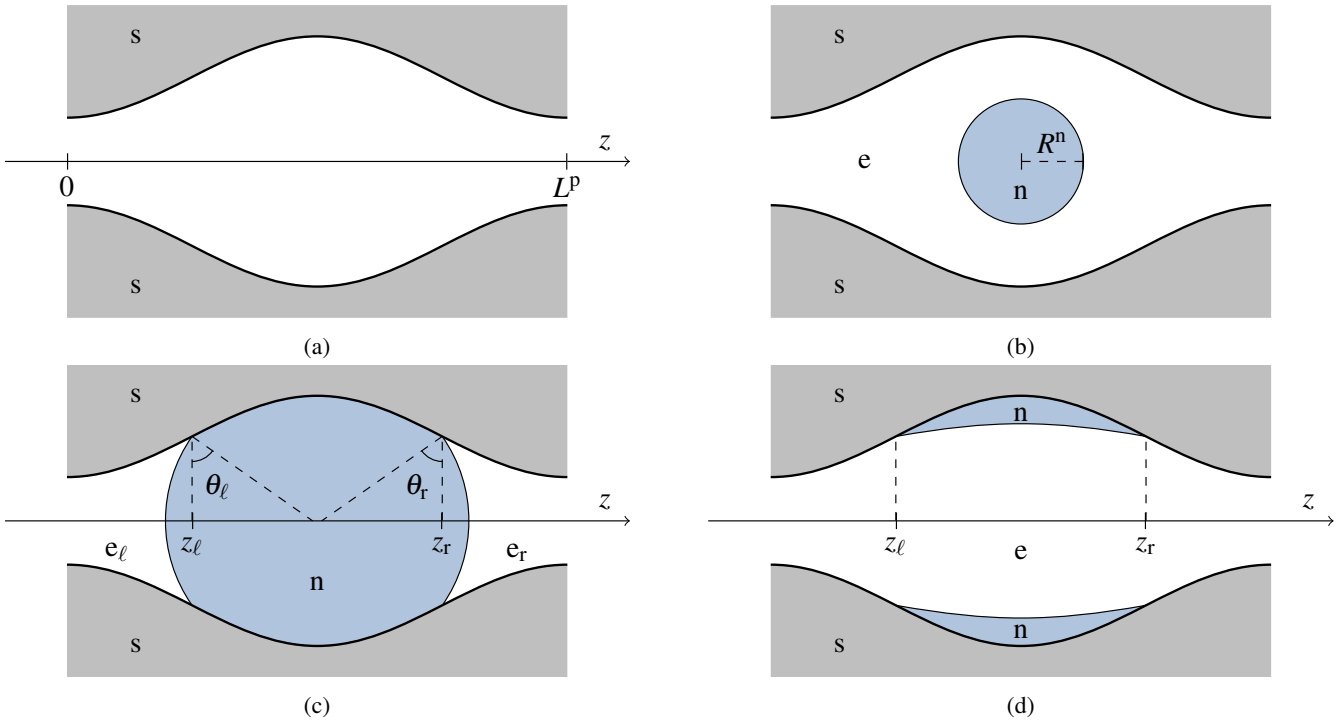

Figure 1: Illustration of the heterogeneous fluid structures under consideration: (a) a homogeneous fluid phase, (b) a free droplet or bubble that is not in contact with the pore walls, (c) a droplet or bubble filling the entire cross-section of some part pore and (d) a thick film of gas or liquid.

thin (α-films) or thick (β-films). In thin films, the thermodynamic properties of the interior deviate from bulk behavior, resulting in a non-zero disjoining pressure. Thin films have been examined by use of theory [23, 24], molecular simulations [25, 26], density functional theory [27] and experiments [28]. A common feature of previous works in the literature discussing the stability of films, is that they consider only stability towards perturbations of the film height. This differs from thermodynamic stability, since exchange of particles is neglected [23, 24]. In this work, we show that the thermodynamic stability of the simplest type of film, the thick film, is very different for closed (canonical ensemble) and open systems (grand canonical ensemble). A new methodology to analyze the thermodynamic stability of films will be presented. This methodology can be extended to include the disjoining pressure and give new insight into thin films in future work.

We will discuss in detail the difference between the thermodynamic stability of heterogeneous structures and equilibrium configurations in *open* and *closed* pores, as well as the influence of pore size. The work is a step towards developing a thermodynamic framework to characterize heterogeneous fluid structures and equilibrium states inside porous media.

We begin by presenting the thermodynamic description of the fluid structures in Section 2. We employ a capillary description, with the rationale that it gives identical results to more sophisticated density functional theory for the thermodynamic stability of multicomponent droplets and bubbles [13]. The numerical methods are described in Section 3, before results are discussed in Section 4. Concluding remarks are provided in Section 5.

2. Models

In the following, we present thermodynamic models for the four systems illustrated in Figure 1. The figure depicts a pore in an incompressible and chemically inert solid matrix. The pore contains a single-component fluid that can have four different configurations, (a) a homogeneous fluid phase, (b) a free droplet or bubble that is not in contact with the pore walls, (c) a droplet or bubble filling the entire cross-section of some part of the pore and (d) a thick film (no disjoining pressure) of gas or liquid. Thin films, that are influenced by a disjoining pressure, are beyond the scope of the present work. By deriving thermodynamic models for all these sub-systems with the same assumptions, it is possible to evaluate their local stability, compare their energies and thus identify the appropriate equilibrium configuration, at given conditions.

We consider a cylindrically symmetric pore of length L^{p} and radius R^{p}. The radius depends on the axial coordinate $z \in [0, L^{\mathrm{p}}]$. Figure 1a illustrates one possible pore geometry, but the governing equations will be derived for an arbitrary function $R^{\mathrm{p}}(z)$, which is sufficiently smooth for $\dot{R}^{\mathrm{p}} = \mathrm{d}R^{\mathrm{p}}/\mathrm{d}z$ and $\ddot{R}^{\mathrm{p}} = \mathrm{d}^2R^{\mathrm{p}}/\mathrm{d}z^2$ to be defined.

For simplicity, we will restrict the pore radii considered in the present work to functions on the form,

$$R^{\mathrm{p}}(z) = L^{\mathrm{p}}\left(0.2 - 0.075\left\{1 + \cos\left(\frac{2\pi z}{L^{\mathrm{p}}}\right)\right\}\right), \tag{1}$$

where Figure 1 shows an example of this profile. It is assumed that the solid matrix acts as a thermal reservoir for the fluids at temperature T.

With the above assumptions, the volume of the pore is constant and can be calculated from,

$$V^{\mathrm{p}} = \pi \int_0^{L^{\mathrm{p}}} (R^{\mathrm{p}})^2 \, \mathrm{d}z. \tag{2}$$

Similarly, the surface area of the solid matrix is constant and equal to

$$A^{\mathrm{p}} = 2\pi \int_0^{L^{\mathrm{p}}} R^{\mathrm{p}} \sqrt{1 + \left(\dot{R^{\mathrm{p}}}\right)^2} \mathrm{d}z. \tag{3}$$

Three interfacial tensions will be parameters in our models. These are σ^{gs}, $\sigma^{\ell \mathrm{s}}$ and $\sigma^{\mathrm{g}\ell}$ for the gas-solid, liquid-solid and gas-liquid interfaces, respectively. In terms of the interfacial tensions, Young's law gives the contact angle α (measured in the liquid) as

$$\cos(\alpha) = \frac{\sigma^{\mathrm{gs}} - \sigma^{\ell \mathrm{s}}}{\sigma^{\mathrm{g}\ell}}. \tag{4}$$

Due to the isothermal conditions, interfacial tensions are assumed to be constant.

The thermodynamic properties of the fluids are described by an equation of state (EOS), where any EOS capable of describing the liquid and gas phases is applicable.

In the following, we present the governing equations for all the sub-systems in Figure 1. A clear distinction is made between whether the system is closed (the canonical ensemble), or connected to a particle reservoir (grand canonical ensemble). The grand canonical ensemble is a natural representation of an open pore, which is equivalent to a system connected to a temperature and pressure reservoir for a single-component system due to the Gibbs–Duhem relation (see [19] for a discussion). Equilibrium in the canonical ensemble is a minimum of the total Helmholtz energy of the system, while equilibrium in the grand canonical ensemble is a minimum of the total grand potential energy. These energy state functions and their stationary states have to be identified for each of the configurations in Figure 1.

2.1. Pore with a homogeneous phase

We start by considering the simplest fluid configuration possible, which is a pore filled with a single-phase fluid. This type of configuration is illustrated in Figure 1a. The Helmholtz energy of this system is

$$F = -pV^{\mathrm{p}} + \mu N + \sigma A^{\mathrm{p}}, \tag{5}$$

where p is the fluid pressure, μ is the chemical potential, N is the number of particles and σ is the interfacial tension between the solid and the fluid, i.e. σ^{gs} for a pore filled with gas and $\sigma^{\ell \mathrm{s}}$ for a pore filled with liquid. The grand potential energy is

$$\Omega = F - \mu N. \tag{6}$$

Since the solid matrix is incompressible, chemically inert and has a constant temperature, its Helmholtz and grand potential energies are constants that can be omitted from the analysis without any further effect on the results. A stationary state of a homogeneous phase is characterized by uniform temperature, pressure and chemical potentials [11]. The phase is thermodynamically stable if its density is within the spinodal limits at the specified temperature. We refer to Aursand et al. [17] for further details on how the spinodal limits can be calculated.

2.2. Pore with a free droplet or bubble

Next, we consider a pore with a free spherical droplet or bubble that is not in contact with the pore walls. The droplet/bubble phase is labeled n, while the surrounding phase is labeled e, as illustrated in Figure 1b.

First, we assume that the pore is a closed system with a fixed total number of particles N, total volume V and temperature T. An equilibrium state of this system is then a minimum in the total Helmholtz energy of the system,

$$F = -p^{\mathrm{e}}V^{\mathrm{e}} + \mu^{\mathrm{e}}N^{\mathrm{e}} + \sigma^{\mathrm{es}}A^{\mathrm{es}} - p^{\mathrm{n}}V^{\mathrm{n}} + \mu^{\mathrm{n}}N^{\mathrm{n}} + \sigma^{\mathrm{en}}A^{\mathrm{en}}. \tag{7}$$

Herein, p^j is the pressure of phase j, μ^j is the chemical potential of phase j and N^j is the number of particles in phase j. The area of the interface between phase i and j is denoted by A^{ij} and the tension of this interface by σ^{ij}. Using that $V^{\mathrm{e}} + V^{\mathrm{n}} = V^{\mathrm{p}}$, $N^{\mathrm{e}} + N^{\mathrm{n}} = N$, $A^{\mathrm{es}} = A^{\mathrm{p}}$ and the Gibbs–Duhem relations for each phase, the differential of F can be written as

$$\mathrm{d}F = -(p^{\mathrm{n}} - p^{\mathrm{e}})\,\mathrm{d}V^{\mathrm{n}} + (\mu^{\mathrm{n}} - \mu^{\mathrm{e}})\,\mathrm{d}N^{\mathrm{n}} + \sigma^{\mathrm{en}}\mathrm{d}A^{\mathrm{en}}. \tag{8}$$

Since the n-phase is assumed to be spherical, A^{en} and V^{n} are not independent. We choose to describe the geometry of the droplet/bubble in terms of its radius R^{n} and get the differential

$$\mathrm{d}F = -\left(p^{\mathrm{n}} - p^{\mathrm{e}} - \frac{2\sigma^{\mathrm{en}}}{R^{\mathrm{n}}}\right) 4\pi (R^{\mathrm{n}})^2 \,\mathrm{d}R^{\mathrm{n}} + (\mu^{\mathrm{n}} - \mu^{\mathrm{e}})\,\mathrm{d}N^{\mathrm{n}}, \tag{9}$$

in terms of perturbations in the independent free variables of the system, R^{n} and N^{n}. The elements in the Jacobian vector of F are then

$$\left(\frac{\partial F}{\partial R^{\mathrm{n}}}\right)_{N^{\mathrm{n}}} = -4\pi (R^{\mathrm{n}})^2 \left(p^{\mathrm{n}} - p^{\mathrm{e}} - \frac{2\sigma^{\mathrm{en}}}{R^{\mathrm{n}}}\right), \tag{10}$$

and

$$\left(\frac{\partial F}{\partial N^{\mathrm{n}}}\right)_{R^{\mathrm{n}}} = \mu^{\mathrm{n}} - \mu^{\mathrm{e}}. \tag{11}$$

A stationary state of F is therefore characterized by equality of the chemical potentials in the two phases and a pressure difference between the gas and liquid given by the Young–Laplace equation. The Hessian matrix of F can be found by further differentiation of the Jacobian, as shown in [13].

Let us now consider the pore in an open system at fixed total volume and temperature that is connected to a particle reservoir, such that the chemical potential of the e-phase is fixed. An equilibrium state is then a minimum of the total grand potential energy of the system,

$$\Omega = F - \mu^{\mathrm{e}}N. \tag{12}$$

By a derivation analogous to that above, one finds the Jacobian vector of Ω and that the criteria for a stationary point in the grand canonical ensemble are exactly the same as in the canonical ensemble. One subtle difference that makes the Hessian matrix of Ω different from that of F, is that μ^{e} in the open system no longer depends on the free variables of the system.

2.3. Pore with an adsorbed droplet or bubble

The next fluid configuration we consider is a pore containing a droplet or a bubble that is in contact with the pore walls and fills the entire pore cross-section for some interval on the z-axis. This type of fluid configuration is illustrated in Figure 1c. The two fluid-fluid interfaces, in contact with the pore walls at z_ℓ and z_r, are assumed to be spherical caps. Again, the droplet/bubble phase is labeled n. The fluid phase on the left side is labeled e_ℓ and the one on the right side is labeled e_r.

The Helmholtz energy is

$$\begin{aligned} F = &- p^{\mathrm{e}_\ell} V^{\mathrm{e}_\ell} + \mu^{\mathrm{e}_\ell} N^{\mathrm{e}_\ell} + \sigma^{\mathrm{es}} A^{\mathrm{e}_\ell \mathrm{s}} + \sigma^{\mathrm{en}} A^{\mathrm{e}_\ell \mathrm{n}} \\ &- p^{\mathrm{e}_\mathrm{r}} V^{\mathrm{e}_\mathrm{r}} + \mu^{\mathrm{e}_\mathrm{r}} N^{\mathrm{e}_\mathrm{r}} + \sigma^{\mathrm{es}} A^{\mathrm{e}_\mathrm{r} \mathrm{s}} + \sigma^{\mathrm{en}} A^{\mathrm{e}_\mathrm{r} \mathrm{n}} \\ &- p^{\mathrm{n}} V^{\mathrm{n}} + \mu^{\mathrm{n}} N^{\mathrm{n}} + \sigma^{\mathrm{ns}} A^{\mathrm{ns}}. \end{aligned} \tag{13}$$

Using now that $V^{\mathrm{e}_\ell} + V^{\mathrm{e}_\mathrm{r}} + V^{\mathrm{n}} = V^{\mathrm{p}}$, $A^{\mathrm{e}_\ell \mathrm{s}} + A^{\mathrm{ns}} + A^{\mathrm{e}_\mathrm{r} \mathrm{s}} = A^{\mathrm{p}}$, $N^{\mathrm{e}_\ell} + N^{\mathrm{n}} + N^{\mathrm{e}_\mathrm{r}} = N$ and that the Gibbs–Duhem relation is satisfied for each phase, we can formulate the differential of F as

$$\begin{aligned} \mathrm{d}F = &- \left(p^{\mathrm{e}_\ell} - p^{\mathrm{n}}\right) \mathrm{d}V^{\mathrm{e}_\ell} + \left(\mu^{\mathrm{e}_\ell} - \mu^{\mathrm{n}}\right) \mathrm{d}N^{\mathrm{e}_\ell} \\ &+ \left(\sigma^{\mathrm{es}} - \sigma^{\mathrm{ns}}\right) \mathrm{d}A^{\mathrm{e}_\ell \mathrm{s}} + \sigma^{\mathrm{en}} \mathrm{d}A^{\mathrm{e}_\ell \mathrm{n}} \\ &- \left(p^{\mathrm{e}_\mathrm{r}} - p^{\mathrm{n}}\right) \mathrm{d}V^{\mathrm{e}_\mathrm{r}} + \left(\mu^{\mathrm{e}_\mathrm{r}} - \mu^{\mathrm{n}}\right) \mathrm{d}N^{\mathrm{e}_\mathrm{r}} \\ &+ \left(\sigma^{\mathrm{es}} - \sigma^{\mathrm{ns}}\right) \mathrm{d}A^{\mathrm{e}_\mathrm{r} \mathrm{s}} + \sigma^{\mathrm{en}} \mathrm{d}A^{\mathrm{e}_\mathrm{r} \mathrm{n}}. \end{aligned} \tag{14}$$

Since both fluid-fluid interfaces are assumed to be shaped like spherical caps, they can each be described by two independent variables. We therefore parameterize the six geometrical quantities V^{e_ℓ}, $A^{\mathrm{e}_\ell \mathrm{s}}$, $A^{\mathrm{e}_\ell \mathrm{n}}$, $V^{\mathrm{e}_\mathrm{r}}$, $A^{\mathrm{e}_\mathrm{r} \mathrm{s}}$, $A^{\mathrm{e}_\mathrm{r} \mathrm{n}}$ in terms of the four independent variables z_ℓ, z_r, θ_ℓ, and θ_r. As illustrated in Figure 1c, z_ℓ denotes the position along the z-axis of the left three-phase contact line of the left meniscus and z_r denotes the position of the contact line of the right meniscus. The angle θ_ℓ is between a line connecting the center of the left sphere with a point on the left three-phase contact line and a line from the same point on the contact line which is perpendicular to the z-axis. The angle θ_r is defined analogously. In terms of the independent variables, we have that

$$V^{\mathrm{e}_\ell} = \pi \int_0^{z_\ell} \left(R^{\mathrm{p}}\right)^2 \mathrm{d}z - \zeta\left(z_\ell, \theta_\ell\right), \tag{15}$$

$$V^{\mathrm{e}_\mathrm{r}} = \pi \int_{z_\mathrm{r}}^{L^{\mathrm{p}}} \left(R^{\mathrm{p}}\right)^2 \mathrm{d}z - \zeta\left(z_\mathrm{r}, \theta_\mathrm{r}\right), \tag{16}$$

$$A^{\mathrm{e}_\ell \mathrm{s}} = 2\pi \int_0^{z_\ell} R^{\mathrm{p}} \sqrt{1 + \left(\dot{R}^{\mathrm{p}}\right)^2} \mathrm{d}z, \tag{17}$$

$$A^{\mathrm{e}_\mathrm{r} \mathrm{s}} = 2\pi \int_{z_\mathrm{r}}^{L^{\mathrm{p}}} R^{\mathrm{p}} \sqrt{1 + \left(\dot{R}^{\mathrm{p}}\right)^2} \mathrm{d}z, \tag{18}$$

$$A^{\mathrm{e}_\ell \mathrm{n}} = \pi \left\{R^{\mathrm{p}}\left(z_\ell\right)\right\}^2 \left\{1 + \xi^2\left(\theta_\ell\right)\right\}, \tag{19}$$

$$A^{\mathrm{e}_\mathrm{r} \mathrm{n}} = \pi \left\{R^{\mathrm{p}}\left(z_\mathrm{r}\right)\right\}^2 \left\{1 + \xi^2\left(\theta_\mathrm{r}\right)\right\}, \tag{20}$$

where

$$\zeta\left(z, \theta\right) = \frac{\pi}{6} \left\{R^{\mathrm{p}}\left(z\right)\right\}^3 \xi\left(\theta\right) \left\{3 + \xi^2\left(\theta\right)\right\}, \tag{21}$$

$$\xi\left(\theta\right) = \frac{1 - \sin\left(\theta\right)}{\cos\left(\theta\right)}. \tag{22}$$

The Helmholtz energy differential may then be expressed as

$$\begin{aligned} \mathrm{d}F = &\left\{\mu^{\mathrm{e}_\ell} - \mu^{\mathrm{n}}\right\} \mathrm{d}N^{\mathrm{e}_\ell} + \left\{\mu^{\mathrm{e}_\mathrm{r}} - \mu^{\mathrm{n}}\right\} \mathrm{d}N^{\mathrm{e}_\mathrm{r}} \\ &+ \left\{\left(\sigma^{\mathrm{es}} - \sigma^{\mathrm{ns}}\right) \frac{\partial A^{\mathrm{e}_\ell \mathrm{s}}}{\partial z_\ell} + \sigma^{\mathrm{en}} \frac{\partial A^{\mathrm{e}_\ell \mathrm{n}}}{\partial z_\ell} - \left(p^{\mathrm{e}_\ell} - p^{\mathrm{n}}\right) \frac{\partial V^{\mathrm{e}_\ell}}{\partial z_\ell}\right\} \mathrm{d}z_\ell \\ &+ \left\{\left(\sigma^{\mathrm{es}} - \sigma^{\mathrm{ns}}\right) \frac{\partial A^{\mathrm{e}_\mathrm{r} \mathrm{s}}}{\partial z_\mathrm{r}} + \sigma^{\mathrm{en}} \frac{\partial A^{\mathrm{e}_\mathrm{r} \mathrm{n}}}{\partial z_\mathrm{r}} - \left(p^{\mathrm{e}_\mathrm{r}} - p^{\mathrm{n}}\right) \frac{\partial V^{\mathrm{e}_\mathrm{r}}}{\partial z_\mathrm{r}}\right\} \mathrm{d}z_\mathrm{r} \\ &+ \left\{\sigma^{\mathrm{en}} \frac{\partial A^{\mathrm{e}_\ell \mathrm{n}}}{\partial \theta_\ell} - \left(p^{\mathrm{e}_\ell} - p^{\mathrm{n}}\right) \frac{\partial V^{\mathrm{e}_\ell}}{\partial \theta_\ell}\right\} \mathrm{d}\theta_\ell \\ &+ \left\{\sigma^{\mathrm{en}} \frac{\partial A^{\mathrm{e}_\mathrm{r} \mathrm{n}}}{\partial \theta_\ell} - \left(p^{\mathrm{e}_\mathrm{r}} - p^{\mathrm{n}}\right) \frac{\partial V^{\mathrm{e}_\mathrm{r}}}{\partial \theta_\mathrm{r}}\right\} \mathrm{d}\theta_\mathrm{r}. \end{aligned} \tag{23}$$

Here, the expressions in the curly brackets are the elements of the Jacobian vector of F. The Hessian matrix can be found by further differentiation of the Jacobian vector.

In a stationary state, all the terms of (23) must vanish. Setting the last two terms equal to zero, yields

$$p^{\mathrm{n}} - p^{\mathrm{e}_\ell} = \frac{2\sigma^{\mathrm{en}} \cos\left(\theta_\ell\right)}{R^{\mathrm{p}}\left(z_\ell\right)}, \tag{24}$$

$$p^{\mathrm{n}} - p^{\mathrm{e}_\mathrm{r}} = \frac{2\sigma^{\mathrm{en}} \cos\left(\theta_\mathrm{r}\right)}{R^{\mathrm{p}}\left(z_\mathrm{r}\right)}. \tag{25}$$

Since the radii of curvature of the fluid-fluid interfaces are $R^{\mathrm{p}}\left(z_\ell\right) / \cos\left(\theta_\ell\right)$ and $R^{\mathrm{p}}\left(z_\mathrm{r}\right) / \cos\left(\theta_\mathrm{r}\right)$, these two equations imply that the interfaces obey the Young–Laplace equation.

For the first two terms in equation (23) to vanish, we must have equality of the chemical potential in all fluid phases. This requires that $p^{\mathrm{e}_\ell} = p^{\mathrm{e}_\mathrm{r}}$, and (24) and (25) may then be combined to give

$$\frac{\cos\left(\theta_\ell\right)}{R^{\mathrm{p}}\left(z_\ell\right)} = \frac{\cos\left(\theta_\mathrm{r}\right)}{R^{\mathrm{p}}\left(z_\mathrm{r}\right)}, \tag{26}$$

meaning that both fluid-fluid interfaces must have the same curvature. The relation between θ_i and the contact angle, measured in the n-phase, is

$$\alpha^{\mathrm{n}} = \theta_i + \beta_i, \tag{27}$$

where

$$\beta_\ell = \arctan\left(\dot{R}^{\mathrm{p}}\left(z_\ell\right)\right), \tag{28}$$

$$\beta_\mathrm{r} = \arctan\left(-\dot{R}^{\mathrm{p}}\left(z_\ell\right)\right). \tag{29}$$

By combining the above equations with (15)-(23) we find by use of trigonometric relations that both contact angles obey Young's equation (4) in a stationary state.

The grand canonical energy Ω of the system is given by (12), where (13) is used for the Helmholtz energy. The derivatives of Ω may then be found by an analogous derivation to that given above. One result from this derivation is that the criteria for a stationary state of Ω are the same as those for a stationary state of F. The Hessian matrix differs, however.

2.4. Pore with a thick film of liquid or gas

The final fluid configuration that will be considered is a pore with a wetting film consisting of either liquid or vapor. The film is considered so thick that interactions between the fluid-fluid and fluid-solid interfaces, as modeled by the disjoining pressure, are negligible. We refer to excellent works in the literature for further information about the disjoining pressure [20–22]. The thick film configuration is illustrated in Figure 1d. As for the adsorbed droplet and bubble, z_ℓ and z_r denote the positions of the left and right three-phase contact lines, respectively.

The Helmholtz energy is now

$$\begin{aligned} F = &- p^\mathrm{e} V^\mathrm{e} + \mu^\mathrm{e} N^\mathrm{e} + \sigma^\mathrm{es} A^\mathrm{es} + \sigma^\mathrm{en} A^\mathrm{en} \\ &- p^\mathrm{n} V^\mathrm{n} + \mu^\mathrm{n} N^\mathrm{n} + \sigma^\mathrm{ns} A^\mathrm{ns}. \end{aligned} \tag{30}$$

The interfacial area between the n- and s-phases is a function of z_ℓ and z_r,

$$A^\mathrm{ns} = 2\pi \int_{z_\ell}^{z_\mathrm{r}} R^\mathrm{p} \sqrt{1 + \left(\dot{R}^\mathrm{p}\right)^2}\,\mathrm{d}z. \tag{31}$$

The volume of the n-phase V^n and the interfacial area between the n- and e-phases A^en depend on z_ℓ and z_r and on the shape of the fluid-fluid interface in between. Since the system is axisymmetric, we may express the shape of the interface by the function $R^\mathrm{f}(z)$, which represents the distance between a point on the fluid-fluid interface to its closest point on the z-axis. The volume V^n and area A^en are then *functionals* of R^f,

$$A^\mathrm{en} = \int_{z_\ell}^{z_\mathrm{r}} L_{A^\mathrm{en}}\left(z, R^\mathrm{f}, \dot{R}^\mathrm{f}\right)\mathrm{d}z, \tag{32}$$

$$V^\mathrm{n} = \int_{z_\ell}^{z_\mathrm{r}} L_{V^\mathrm{n}}\left(z, R^\mathrm{f}, \dot{R}^\mathrm{f}\right)\mathrm{d}z. \tag{33}$$

The integrands of these functionals are

$$L_{A^\mathrm{en}}\left(z, R^\mathrm{f}, \dot{R}^\mathrm{f}\right) = 2\pi R^\mathrm{f} \sqrt{1 + \left(\dot{R}^\mathrm{f}\right)^2}, \tag{34}$$

$$L_{V^\mathrm{n}}\left(z, R^\mathrm{f}, \dot{R}^\mathrm{f}\right) = \pi\left\{(R^\mathrm{p})^2 - \left(R^\mathrm{f}\right)^2\right\}. \tag{35}$$

Using that $A^\mathrm{es} + A^\mathrm{ns} = A^\mathrm{p}$, $V^\mathrm{e} + V^\mathrm{n} = V^\mathrm{p}$ and $N^\mathrm{e} + N^\mathrm{n} = N$ we proceed to eliminate A^es, V^e and N^e from (30) and get

$$\begin{aligned} F = \; &(\mu^\mathrm{n} - \mu^\mathrm{e})\, N^\mathrm{n} - p^\mathrm{e} V^\mathrm{p} + \sigma^\mathrm{es} A^\mathrm{p} + \mu^\mathrm{e} N \\ &- (p^\mathrm{n} - p^\mathrm{e})\, V^\mathrm{n} + (\sigma^\mathrm{ns} - \sigma^\mathrm{es})\, A^\mathrm{ns} + \sigma^\mathrm{en} A^\mathrm{en}. \end{aligned} \tag{36}$$

Taking the differential on both sides of (36) gives

$$\begin{aligned} dF = \; &(\mu^\mathrm{n} - \mu^\mathrm{e})\, dN^\mathrm{n} - (p^\mathrm{n} - p^\mathrm{e})\, dV^\mathrm{n} \\ &+ (\sigma^\mathrm{ns} - \sigma^\mathrm{es})\, dA^\mathrm{ns} + \sigma^\mathrm{en} dA^\mathrm{en}. \end{aligned} \tag{37}$$

The above equation shows that in a stationary state, the chemical potentials of the e- and n-phases must be the same. The Helmholtz energy of a film in a pore with a uniform chemical potential (subscript μ) can be formulated as

$$\begin{aligned} F_\mu = F_\mu^\circ + \pi \int_{z_\ell}^{z_\mathrm{r}} &2\sigma^\mathrm{en} R^\mathrm{f} \sqrt{1 + \left(\dot{R}^\mathrm{f}\right)^2} \\ &- (p^\mathrm{n} - p^\mathrm{e})\left\{(R^\mathrm{p})^2 - \left(R^\mathrm{f}\right)^2\right\} \\ &+ 2\,(\sigma^\mathrm{ns} - \sigma^\mathrm{es})\, R^\mathrm{p} \sqrt{1 + \left(\dot{R}^\mathrm{p}\right)^2}\,\mathrm{d}z. \end{aligned} \tag{38}$$

where we have integrated (37) and used (32) and (33). F_μ° is a constant. To have a stationary state in F_μ, the first variation with respect to the function R^f must vanish and R^f must therefore satisfy the Euler–Lagrange equation in the interval $z \in (z_\ell, z_\mathrm{r})$. The Euler–Lagrange equation leads to the following second-order ordinary differential equation (ODE) for R^f,

$$p^\mathrm{e} - p^\mathrm{n} = \sigma^\mathrm{en}\,(\kappa_1 + \kappa_2), \tag{39}$$

where

$$\kappa_1 = \frac{1}{R^\mathrm{f}\left(1 + \left(\dot{R}^\mathrm{f}\right)^2\right)^{\frac{1}{2}}}, \tag{40}$$

$$\kappa_2 = -\frac{\ddot{R}^\mathrm{f}}{\left(1 + \left(\dot{R}^\mathrm{f}\right)^2\right)^{\frac{3}{2}}}, \tag{41}$$

are the interfacial curvatures. This ODE can be recognized as the Young–Laplace relation for the film. Since (39) is a second-order ODE, we need boundary conditions on both R^f and $\dot{R}^\mathrm{f}$ at the free end points, z_ℓ and z_r to fully define the film. The boundary conditions on R^f are $R^\mathrm{f}(z_\ell) = R^\mathrm{p}(z_\ell)$ and $R^\mathrm{f}(z_\mathrm{r}) = R^\mathrm{p}(z_\mathrm{r})$. To derive boundary conditions for $\dot{R}^\mathrm{f}$, we must consider the *transversal conditions* at the free end points z_ℓ and z_r, see e.g. page 159 in [29]. They give that

$$\cos(\alpha^\mathrm{n}) = \frac{\sigma^\mathrm{es} - \sigma^\mathrm{ns}}{\sigma^\mathrm{en}}, \tag{42}$$

must be satisfied at the end points z_ℓ and z_r. Here, α^n is the contact angle measured in the film. The transversal conditions are thus satisfied when the three-phase contact angles obey Young's equation, like the adsorbed droplet/bubble.

The grand canonical energy Ω of the pore with a film is given by (12), where (30) is used for the Helmholtz energy. As for the other systems, the criteria for a stationary state of Ω are the same as those for a stationary state of F. To analyze the thermodynamic stability of the film, one possibility is to study the second variation of e.g. F at the stationary state. As this is often challenging due to the infinite number of possible functions that can perturb the stationary state, we present in Section 3 a new methodology to analyze the stationary states of films.

3. Numerical methods

In this section, we provide details on the numerical methods used to determine the stationary states and the thermodynamic

stability of the configurations in Figure 1. For all the heterogeneous structures, one way to identify stationary states is to first determine the shape and positions of the interfaces. The outcome is a fixed value of the pressure difference $\Delta p = p^{\mathrm{e}} - p^{\mathrm{n}}$. For the film, this can be done by solving the Euler–Lagrange equation (39) as described in Section 3.2. Subsequently, one can calculate the phase equilibrium with specified $\Delta p = p^{\mathrm{e}} - p^{\mathrm{n}}$, as described in Section 3.1.

3.1. Phase equilibrium calculations

All the heterogeneous structures considered in this work are characterized by the same chemical potentials in the n- and e-phases, but at a fixed pressure difference $\Delta p = p^{\mathrm{e}} - p^{\mathrm{n}}$, temperature T and phase volumes V^{e} and V^{n}. This poses an untypical phase-equilibrium problem.

To determine the remaining thermodynamic properties of the system, one can solve for the dimensionless particle numbers N^{n}/N° and N^{e}/N°. This procedure amounts to solving the nonlinear system of equations $\mathbf{F}\left(N^{\mathrm{n}}/N^{\circ}, N^{\mathrm{e}}/N^{\circ}\right) = \mathbf{0}$, where

$$\mathbf{F}\left(\frac{N^{\mathrm{n}}}{N^{\circ}}, \frac{N^{\mathrm{e}}}{N^{\circ}}\right) = \begin{bmatrix} \frac{\mu^{\mathrm{e}}(T,V^{\mathrm{e}},N^{\mathrm{e}}) - \mu^{\mathrm{n}}(T,V^{\mathrm{e}},N^{\mathrm{e}})}{RT} \\ \frac{p^{\mathrm{e}}(T,V^{\mathrm{e}},N^{\mathrm{e}}) - p^{\mathrm{n}}(T,V^{\mathrm{e}},N^{\mathrm{e}}) - \Delta p}{p^{\circ}} \end{bmatrix}. \tag{43}$$

Herein, the functions for pressure and chemical potentials, and the derivatives required to compute the Jacobian matrix of $\mathbf{F}$, are provided by the EOS. The scaling parameters are

$$p^{\circ} = 10^5 \text{ Pa}, \tag{44}$$

$$N^{\circ} = \frac{p^{\circ} V^{\mathrm{p}}}{RT}, \tag{45}$$

and R is the universal gas constant. The system in (43) was solved using Newton's method. Initial guesses for N^{n} and N^{e} were obtained from a standard phase equilibrium calculation [17, 30–32] at the specified temperature and saturation pressure. The EOS implementation used was provided by our in-house thermodynamic library presented by Wilhelmsen et al. [33].

3.2. Solving the film Euler–Lagrange equation

The ODE in (39) gives a requirement on the film profile that must be satisfied to have a vanishing first variation of the Helmholtz and grand canonical energies. Since the ODE is second-order and requires boundary conditions on both R^{f} and $\dot{R}^{\mathrm{f}}$ at z_ℓ and z_{r}, it represents a two-point boundary value problem. We solved this problem using the shooting method. The solution strategy was to first specify the position z_ℓ. Since the contact angle and pore radius at z_ℓ are known, R^{f} and $\dot{R}^{\mathrm{f}}$ are also specified. Next, a search was performed for the values of the variables $\Delta p = p^{\mathrm{e}} - p^{\mathrm{n}}$ and z_{r} that satisfy the two boundary conditions on R^{f} and $\dot{R}^{\mathrm{f}}$ at z_{r}. The shooting procedure thus amounts to solving $\mathbf{G}\left(\Delta p/p^{\circ}, z_{\mathrm{r}}/L^{\mathrm{p}}\right) = \mathbf{0}$, where

$$\mathbf{G}\left(\frac{\Delta p}{p^{\circ}}, \frac{z_{\mathrm{r}}}{L^{\mathrm{p}}}\right) = \begin{bmatrix} \frac{R^{\mathrm{f}}(z_{\mathrm{r}}) - R^{\mathrm{p}}(z_{\mathrm{r}})}{L^{\mathrm{p}}} \\ \frac{\dot{R}^{\mathrm{f}}(z_{\mathrm{r}}) - \tan(\theta_{\mathrm{r}})}{\max(1, |\tan(\theta_{\mathrm{r}})|)} \end{bmatrix}, \tag{46}$$

and

$$\theta_{\mathrm{r}} = \arctan\left(\dot{R}^{\mathrm{p}}\left(z_{\mathrm{r}}\right)\right) + \alpha^{\mathrm{n}}. \tag{47}$$

The scaling parameter is

$$p^{\circ} = \frac{\sigma^{\mathrm{en}}}{L^{\mathrm{p}}}. \tag{48}$$

One evaluation of $\mathbf{G}$ involves one integration of (39). We used `odeint` from `scipy`'s `integrate` module for the ODE integrations and `fsolve` from the `optimize` module to solve $\mathbf{G} = \mathbf{0}$ [34].

A complicating factor in the search for stationary states is that there may be many solutions to $\mathbf{G} = \mathbf{0}$ with the same z_ℓ. In practice, however, we have found that we can identify the one that is potentially stable and discard any other solutions in subsequent analysis. This is further explained in Appendix A.

3.3. A discrete method for describing the film

The variational formulation works well for identifying stationary states in F and Ω, where the Euler–Lagrange equation for the film (39) can be solved as described in Section 3.2. The procedure identifies stationary states, but it does not give any insight into the thermodynamic stability of the film. This information is contained in the second variation (or higher-order variations, if the second variation happens to be zero). For a stationary state of a functional to be a minimum, it is necessary to have a positive second variation for all viable perturbations, as discussed by Wilhelmsen et al. [13]. To establish that this is the case, or not, can be very demanding and it is impossible for many examples.

In this section, we present a new methodology for analyzing the thermodynamic stability of films. The approach that we follow here is to discretize the functionals for A^{en} (32) and V^{n} (33) and use the discretized functionals to represent the Helmholtz and grand canonical energies. The functionals are integrated numerically using a quadrature rule over a predefined grid, where the end-points are left unspecified. This transforms the variational problem of minimizing F or Ω in the space of functions R^{f}, to an algebraic problem where F is to be minimized by a vector in $\mathbb{R}^M$. Local stability can then be evaluated by considering the eigenvalues of a Hessian matrix.

This procedure can be applied to general problems in functional optimization. We have tested it carefully and successfully reproduced well-known results from variational calculus, such as the Brachistochrone and the hanging cable problems [29], see supplementary material.

In the discrete formulation of the film, we approximate the function R^{f} by the vector

$$\mathbf{R}^{\mathrm{f}} = \left[R_1^{\mathrm{f}}, R_2^{\mathrm{f}}, ..., R_M^{\mathrm{f}}\right]^{\mathrm{T}}, \tag{49}$$

which represents the values of R^{f} at points on a predefined gird with M points on the z-axis, given by

$$\mathbf{z} = \left[z_1, z_2, ..., z_M\right]^{\mathrm{T}}. \tag{50}$$

The complete vector of geometrical unknowns, including the positions of the free end points, is then

$$\mathbf{x} = [x_1, x_2, ..., x_{M+2}]^{\mathrm{T}}, \tag{51}$$

$$= \left[z_\ell, z_\mathrm{r}, R_1^\mathrm{f}, R_2^\mathrm{f}, ..., R_M^\mathrm{f}\right]^{\mathrm{T}}. \tag{52}$$

The volume V^n and area A^ne can now be approximated by the midpoint rule,

$$V^\mathrm{n}(\mathbf{x}) = \sum_{i=0}^{M} L_{V^\mathrm{n}}\left(\bar{z}_i, \bar{R}_i^\mathrm{f}, \dot{\bar{R}}_i^\mathrm{f}\right)\Delta z_i, \tag{53}$$

$$A^\mathrm{en}(\mathbf{x}) = \sum_{i=0}^{M} L_{A^\mathrm{en}}\left(\bar{z}_i, \bar{R}_i^\mathrm{f}, \dot{\bar{R}}_i^\mathrm{f}\right)\Delta z_i. \tag{54}$$

The integrands L_{V^n} and L_{A^en} are given by (35) and (34), respectively, and

$$\bar{z}_i = \frac{z_{i+1} + z_i}{2}, \tag{55}$$

$$\bar{R}_i^\mathrm{f} = \frac{R_{i+1}^\mathrm{f} + R_i^\mathrm{f}}{2}, \tag{56}$$

$$\dot{\bar{R}}_i^\mathrm{f} = \frac{R_{i+1}^\mathrm{f} - R_i^\mathrm{f}}{\Delta z_i}, \tag{57}$$

$$\Delta z_i = z_{i+1} - z_i, \tag{58}$$

In addition, $R_0^\mathrm{f} = R^\mathrm{p}(z_\ell)$, $R_{M+1}^\mathrm{f} = R^\mathrm{p}(z_\mathrm{r})$, $z_0 = z_\ell$ and $z_{M+1} = z_\mathrm{r}$.

The discretized Helmholtz energy for the film can now be calculated by introducing into (36) the discrete functionals $V^\mathrm{n}(\mathbf{x})$ and $A^\mathrm{en}(\mathbf{x})$, and the interfacial area $A^\mathrm{ns}(z_\ell, z_\mathrm{r})$ as given by (31),

$$\begin{aligned} F(\mathbf{y}) = {} & \{\mu^\mathrm{n} - \mu^\mathrm{e}\}N^\mathrm{n} - p^\mathrm{e}V^\mathrm{p} + \sigma^\mathrm{es}A^\mathrm{p} + \mu^\mathrm{e}N + \sigma^\mathrm{en}A^\mathrm{en}(\mathbf{x}) \\ & - \{p^\mathrm{n} - p^\mathrm{e}\}V^\mathrm{n}(\mathbf{x}) + \{\sigma^\mathrm{ns} - \sigma^\mathrm{es}\}A^\mathrm{ns}(z_\ell, z_\mathrm{r}). \end{aligned} \tag{59}$$

Since, the quantities V^n, A^ns and A^ne depend only on the variables contained in $\mathbf{x}$, and since V^p, A^p and N are constants, the free variables of the system are the elements of $\mathbf{x}$ and the number of particles in the film N^n,

$$\mathbf{y} = [y_1, y_2, ..., y_{M+3}]^{\mathrm{T}},$$

$$= \left[N^\mathrm{n}, z_\ell, z_\mathrm{r}, R_1^\mathrm{f}, R_2^\mathrm{f}, ..., R_M^\mathrm{f}\right]^{\mathrm{T}}. \tag{60}$$

The elements of the Jacobian vector can be obtained from (37) as

$$\frac{\partial F}{\partial y_1} = \mu^\mathrm{n} - \mu^\mathrm{e}, \tag{61}$$

and, for $i \in [2, ..., M+3]$,

$$\frac{\partial F}{\partial y_i} = -(p^\mathrm{n} - p^\mathrm{e})\frac{\partial V^\mathrm{n}}{\partial y_i} + (\sigma^\mathrm{ns} - \sigma^\mathrm{es})\frac{\partial A^\mathrm{ns}}{\partial y_i} + \sigma^\mathrm{ne}\frac{\partial A^\mathrm{ne}}{\partial y_i}. \tag{62}$$

The Hessian matrix can be found by further differentiation. The procedure used for calculating the derivatives of V^n and A^ne w.r.t. y_i is documented in the supplementary material. By a derivation similar to that above, we obtain the grand potential Ω, its Jacobian vector and its Hessian matrix.

The strategy to solve the discrete problem is to use the stationary state obtained from solving the ODE as described in Section 3.2 as initial guess. The stationary state for the discrete problem is then found by solving for the vector $\mathbf{y}^*$ for which the discrete Jacobian vector is zero,

$$\left.\frac{\mathrm{d}F}{\mathrm{d}\mathbf{y}}\right|_{\mathbf{y}^*} = \mathbf{0}. \tag{63}$$

Since we have an expression for the Hessian matrix of F and a very good initial guess for the solution to (63), this nonlinear system of equations is solved with Newton's method with few number of iterations. A convergence study is reported in Appendix B, which shows that the film profiles obtained by the discrete method converge to those obtained by solving the Euler–Lagrange equation as the grid size M is increased. For a thorough exposition of the discrete approach, we refer to the supplementary material.

3.4. Stability analysis

Any stationary state identified using the procedures described above, and defined by the vector $\mathbf{y}^*$, will be stationary for both F and Ω and, therefore, in both a closed and an open pore. Since the Jacobian vector is $\mathbf{0}$, the change in, say, F in response to a small perturbation $\mathrm{d}\mathbf{y}$ of $\mathbf{y}^*$ can be expressed as

$$\mathrm{d}F = \mathrm{d}\mathbf{y}^{\mathrm{T}}\left.\frac{\mathrm{d}^2F}{\mathrm{d}\mathbf{y}^2}\right|_{\mathbf{y}^*}\mathrm{d}\mathbf{y}, \tag{64}$$

where $\mathrm{d}^2F/\mathrm{d}\mathbf{y}^2$ is the Hessian matrix. For the film, we calculate the Hessian matrices using the discrete description, see Section 3.3. The symmetric Hessian matrix can be decomposed into

$$\left.\frac{\mathrm{d}^2F}{\mathrm{d}\mathbf{y}^2}\right|_{\mathbf{y}^*} = \mathbf{Q}\mathbf{\Lambda}\mathbf{Q}^{\mathrm{T}}, \tag{65}$$

where $\mathbf{\Lambda}$ is the diagonal matrix eigenvalues and $\mathbf{Q}$ is a matrix where column i is the eigenvector $\mathbf{q}_i$ (with unit length in the L_2-norm) associated with eigenvalue λ_i. The eigenvectors are orthogonal, since the Hessian is symmetric.

A stationary state $\mathbf{y}^*$ corresponds to a minimum in F and is considered locally stable in the closed pore if all eigenvalues of the Hessian are positive. If one or more of the eigenvalues are negative, $\mathrm{d}\mathbf{y}$ can be taken in direction of the corresponding eigenvectors $\mathbf{q}_i$ (or $-\mathbf{q}_i$) to give a negative $\mathrm{d}F$. The stationary state is thus not a minimum in the Helmholtz energy and it is therefore unstable. Analogous considerations apply for Ω and stability in open pores.

The eigenvectors that correspond to the negative eigenvalues give information about the direction of the perturbations that lead to a reduction in the energy and make the system unstable. For both the adsorbed droplet/bubble and the films, we observe (see Section 4) two distinct classes of instabilities that we name (1) translation and (2) condensation/evaporation. Translation instabilities are perturbations where the n-phase moves along the z-axis and only a small number of particles are transferred

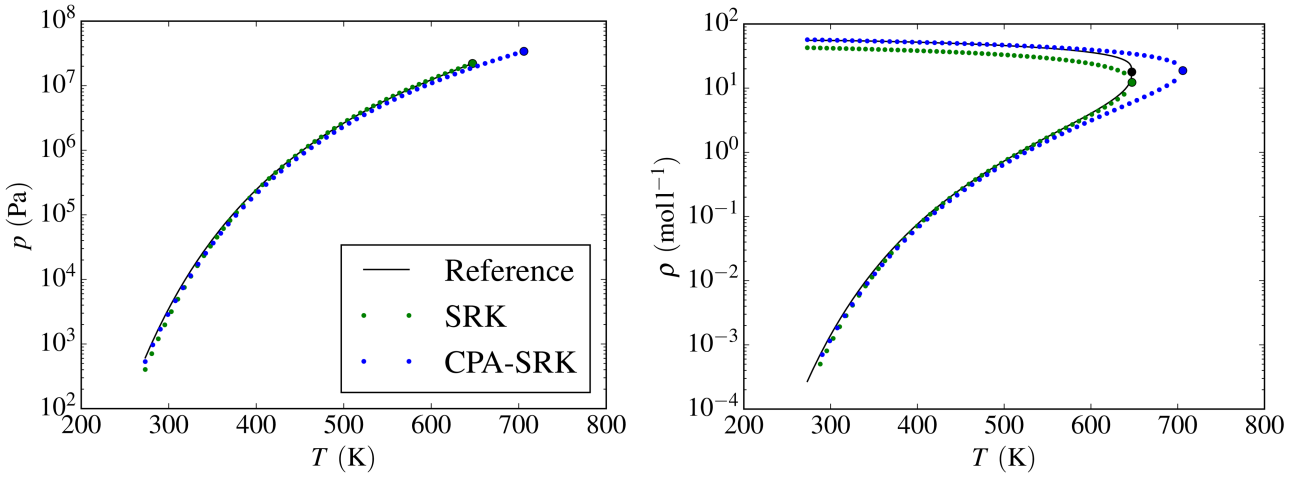

(a) (b)

Figure 2: Saturation properties of water, as predicted by SRK (green) and CPA-SRK (blue). Reference data from [35] are shown for comparison (black). Compared to SRK, CPA-SRK is more inaccurate in the critical region, but has superior predictions of liquid densities in the temperatures around 300 K.

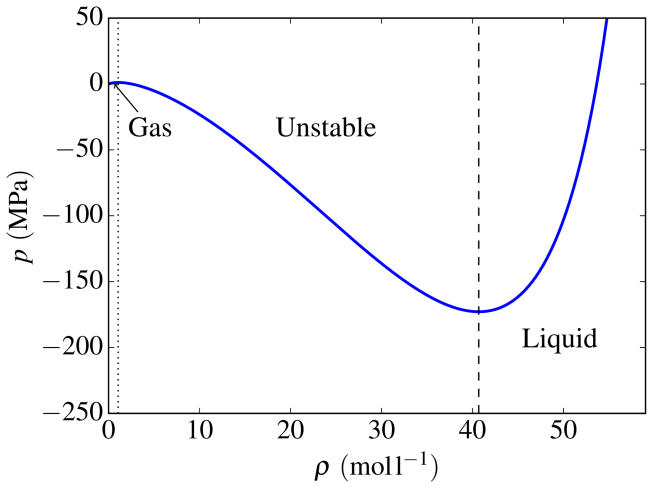

Figure 3: CPA-SRK isotherm (solid blue) for water at 358 K. The densities at the gas spinodal (dotted line) and liquid spinodal (dashed line) are also indicated. Phases with densities between the two spinodals are unstable.

to/from the e-phase(s). For condensation/evaporation instabilities on the other hand, the n-phase expands or contracts while exchanging particles with the e-phase(s), without shifting its center of mass.

Eigenvectors and eigenvalues were calculated using `eigh` from `numpy`'s `linalg` module [34]. This function uses the `*syevd` routines from LAPACK, which compute the eigenvalues and eigenvectors of symmetric matrices [36].

4. Results

In the following, we will discuss the thermodynamic stability of the heterogeneous structures illustrated in Figure 1. The focus will be on the influence of pore size, the fluid-solid interaction, as captured by a finite contact angle α, and the difference in thermodynamic stability between closed and open systems. We restrict the discussion to two pore sizes, $L^{\mathrm{p}} = 10\,\mu\mathrm{m}$ and $L^{\mathrm{p}} = 0.01\,\mu\mathrm{m}$. Despite the small size of both pores, we will refer to the 10 µm-pore as large and the 0.01 µm-pore as small.

Water at 358 K will be used as example, inspired by the operational conditions of a proton-exchange membrane fuel cell[1] [37]. The thermodynamic properties of water are described by the cubic-plus-association modification to the Soave–Redlich–Kwong EOS (CPA-SRK). In Figure 2, the saturation properties of water as described by both the Soave–Redlich–Kwong EOS (SRK) and CPA-SRK are plotted together with reference data from [35]. Compared to SRK, CPA-SRK is more inaccurate in the critical region, but has superior prediction of liquid densities at lower temperatures and is therefore the preferred choice here.

The CPA-SRK isotherm for water at 358 K is shown in Figure 3, where the gas and liquid spinodals are indicated by vertical lines. A homogeneous phase with a density between the two spinodals is thermodynamically unstable. The isotherm shows that the EOS predicts stable or metastable stretched liquid phases down to pressures of −173 MPa, consistent with the findings of Caupin et al. [5] and Azouzi et al. [6].

In the models presented in Section 2, the energies of the gas-liquid interface $\sigma^{\mathrm{g}\ell}$, the gas-solid interface σ^{gs} and the liquid-solid interface $\sigma^{\ell\mathrm{s}}$ are necessary input parameters. The gas-liquid surface tension of water at 358 K is $0.0616\,\mathrm{N\,m^{-1}}$ [35]. With this value in place, it is only the difference between the gas-solid and gas-liquid interfacial tensions that is of physical significance in the models. We therefore set $\sigma^{\ell\mathrm{s}} = 0$ and subsequently use $\sigma^{\mathrm{g}\ell}$ and the specified contact angle α to calculate σ^{gs} by use of Young's equation (4).

[1] Condensation of liquid water in such fuel cells may block reactant flow paths and is severely detrimental to their performance. It is therefore of interest to know if, say, a path-blocking adsorbed droplet or a liquid film is the equilibrium configuration under the chosen operating conditions.

4.1. Pore with a free droplet or bubble

The thermodynamic stability of free droplets and bubbles in a closed pore has been studied in previous works [16, 18, 19]. Our results for water at 358 K are shown in Figure 4. The stability is here mapped out in terms of the relative droplet/bubble size $R^{\mathrm{n}}/L^{\mathrm{p}}$ and contact angle α. The largest bubble radius that has been considered equals the radius of the pore at the widest point.

As expected, the thermodynamic stability of free bubbles and droplets is independent of contact angle. For both pore sizes, large bubbles and droplets are stable and have lower Helmholtz energies than if the pores were filled with a homogeneous phase (with the same number of particles). As R^{n} decreases however, the configurations first become metastable with respect to the homogeneous phase and, eventually, unstable. The reason is that, as the volume of the n-phase becomes smaller, the reduction in energy from having both a liquid and a gas phase does not compensate for the energy cost of the gas-liquid interface. These findings are consistent with those of Wilhelmsen et al. [13]. They considered droplets and bubbles in a spherical container, where the interfacial energy between the container and the e-phase was zero. The non-zero energy of the es-interface adds a constant term to the Helmholtz energy that does not change the local stability w.r.t. to the analysis performed by Wilhelmsen et al. [13]. This is also the reason why the contact angle does not affect stability. However, it is necessary to include the contribution from the fluid-solid interface when comparing the energy of the free droplet/bubble configurations with other configurations such as adsorbed droplet/bubbles and films.

The thermodynamic stability of free droplets and bubbles in a closed system changes with pore size, which can be seen by comparing Figure 4a with 4b for the droplets and Figure 4c with 4d for the bubbles. In the white region in the bottom part of the figures, the droplet and bubble radius becomes so small that the pressure difference needed to satisfy the Young–Laplace relation is too large to conform with equal chemical potential between the phases. The limiting factor for the droplets is the gas spinodal and for the bubbles it is the liquid spinodal. The density range where the bubbles and droplets are thermodynamically stable (the green regions) or metastable (orange regions) decreases with pore size. This is due to the superstabilization of the homogeneous phase that occurs in small pores. We refer to [18] for an elaborate discussion of this topic.

The white dashed and dotted lines in Figure 4 mark the states where the total density in the pore reaches the spinodal limits, and the homogeneous fluid becomes unstable. Beyond this limit, the fluid will spontaneously decompose into two phases.

In agreement with previous work, we find that free droplets and bubbles are unstable in the open systems [16], also in the presence of a solid-fluid interface.

4.2. Pore with an adsorbed droplet or bubble

When the solid-fluid interfacial energy is lower than the gas-liquid interfacial tension, the bubbles and droplets can lower their energies by adsorbing to the pore walls, as shown in Figure 1c. The thermodynamic stability of adsorbed bubbles and droplets is mapped out in Figure 5 in terms of the position of the left meniscus z_ℓ and the contact angle α for open and closed pores with lengths 10 μm and 0.01 μm.

In contrast to the free droplets and bubbles, the absorbed droplets and bubbles can be stable both in open and closed pores. The general trend is that adsorbed droplets are thermodynamically stable if the liquid contact angle is high (non-wetting), while bubbles are stable when the liquid contact angle is low (wetting), and the range of stability depends on the value of the contact angle. We find that this behavior depends strongly on the pore geometry. An in-depth discussion of the influence of pore morphology on the thermodynamic stability however, is beyond the scope of the present work.

We have analyzed in detail the regions where the adsorbed droplets and bubbles become unstable. The eigenvectors associated with the negative Hessian eigenvalues in these regions reveal that an instability w.r.t. to translation of the n-phase along the z-axis, i.e. a mechanical instability, is present in the unstable regions of all the adsorbed bubble and droplet configurations. A perturbation of the position of the droplet/bubble leads to a net force that moves it further in the direction of the perturbation, not back to the original position as for the stable droplets/bubbles. The Hessian matrices of the open systems have an additional negative eigenvalue in the unstable regions. The second negative eigenvalue is associated with condensation/evaporation. This instability is also present for the droplet in the small closed pore, when the liquid pressures become large and negative. We have included figures that display where these instabilities appear in the supplementary material. Comparing the stability regions of the droplets (left column in Figure 5) with those of the bubbles (right column Figure 5), these are clearly anti-symmetric. This is because the droplets with contact angles α are mechanically identical to bubbles with contact angle $\pi - \alpha$.

The white regions in the stability maps for the 10 μm-pore represent configurations where no stationary state can be found because the two menisci would have intersected or extended outside the pore. Such configurations are unfeasible and are not considered in the analysis. The same is true for the small pores. In addition, the large curvatures of some menisci in the small pores result in large, negative liquid pressures. Figure 3 shows that the liquid spinodal poses a lower limit to how large the negative pressures of the liquid phase can be. Configurations with a lower pressure than the liquid spinodal are unfeasible.

Figure 5e shows results for a closed pore of the small kind containing an adsorbed droplet. It has a considerable region where the droplets are metastable w.r.t. a pore with a homogeneous liquid phase (with the same number of particles). In a large closed pore, the thermodynamic stability map looks the same, except that the metastable region is stable. A figure can be found in the supplementary material. The reason for the appearance of the metastable region in the small pore is as for the free droplet/bubble; when the volumes of the bulk phases become smaller, the reduction in energy from having both a gas and a liquid does not compensate for the energy associated with the gas-liquid interface. The adsorbed bubble configurations display a similar behavior, where large bubbles (relative

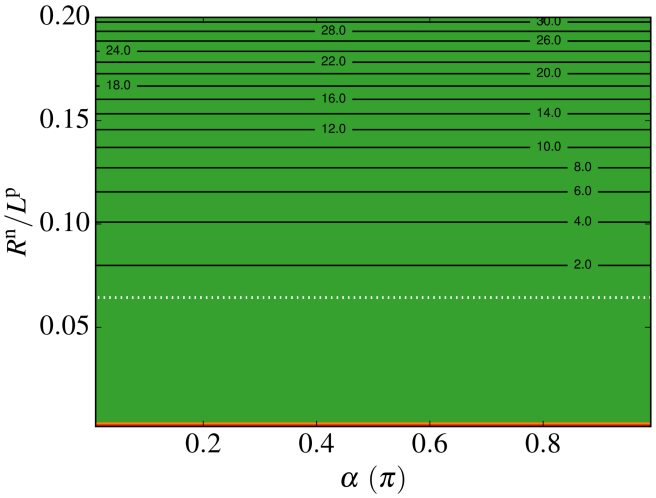

(a) Free droplets in closed pore of 10 µm

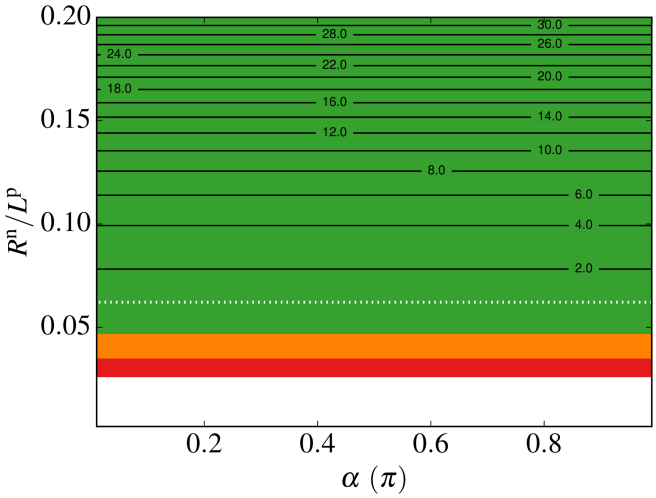

(b) Free droplets in closed pore of 0.01 µm

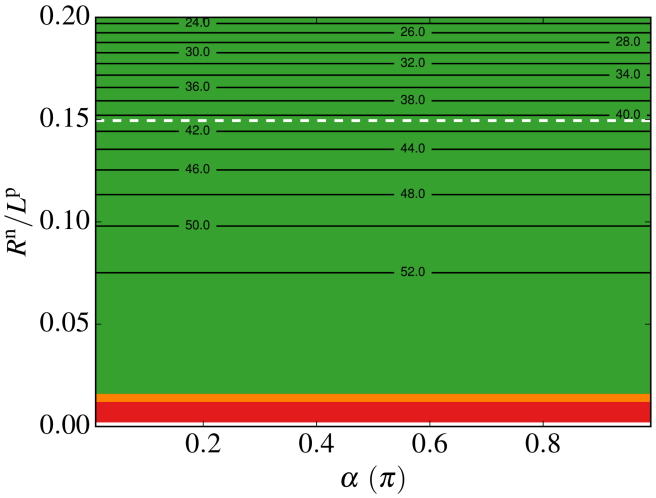

(c) Free bubbles in closed pore of 10 µm

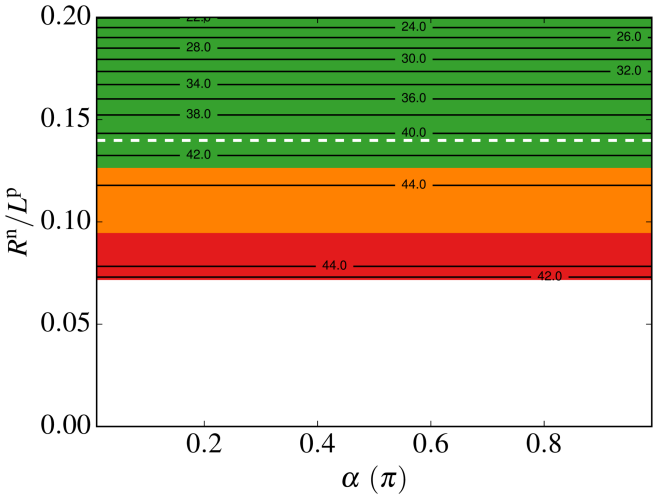

(d) Free bubbles in closed pore of 0.01 µm

Figure 4: Stability maps for (a), (b) free droplets and (c), (d) free bubbles in closed pores of lengths (a), (c) 10 µm and (b), (d) 0.01 µm. The black contour lines indicate the total fluid density in mol l^{-1}. Unstable configurations are red, stable configurations are green and configurations that are locally stable, but have a larger Helmholtz energy than if the pore were filled with a single homogeneous phase, are orange. The gas spinodal density of 1.05 mol l^{-1} is drawn as a dotted white line and the liquid spinodal of 40.7 mol l^{-1} is shown as a dashed white line. No homogeneous phase filling the entire pore can exist for densities between the spinodals.

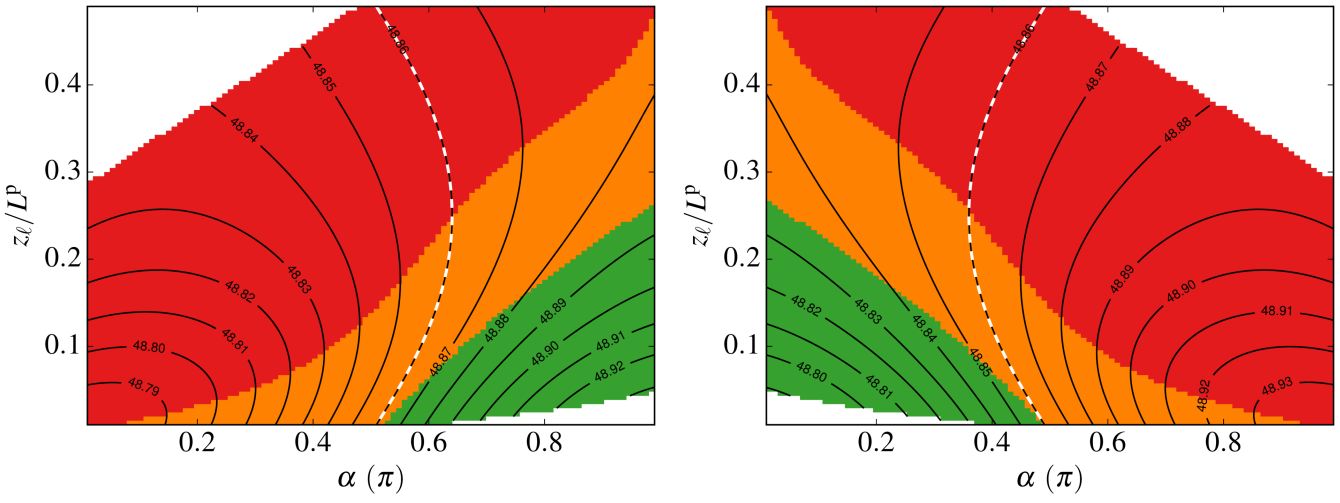

(a) Adsorbed droplet in open pore of 10 µm

(b) Adsorbed bubbles in open pore of 10 µm

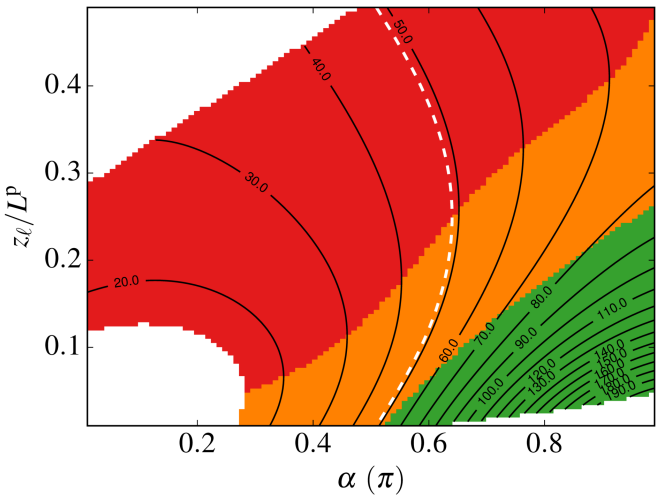

(c) Adsorbed droplets in open pore of 0.01 µm

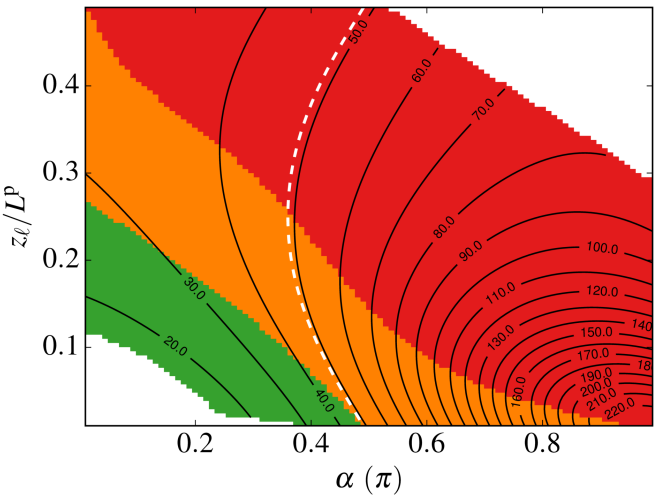

(d) Adsorbed bubbles in open pore of 0.01 µm

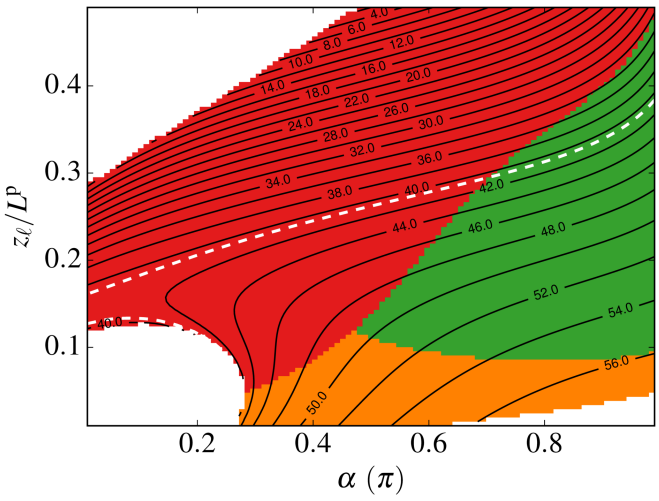

(e) Adsorbed droplets in closed pore of 0.01 µm

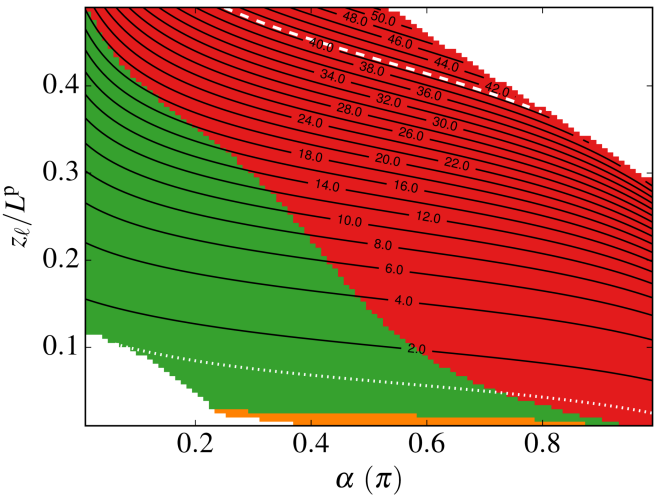

(f) Adsorbed bubbles in closed pore of 0.01 µm

Figure 5: Stability maps of (left column) adsorbed droplets and (right column) adsorbed bubbles in open and closed pores with lengths 10 µm and 0.01 µm. For the closed pores, the black contour lines indicate the total fluid density in mol l^{-1}. Further, the gas spinodal density of 1.05 mol l^{-1} is drawn as a dotted white line and the liquid spinodal of 40.7 mol l^{-1} is shown as a dashed white line. No homogeneous phase filling the entire pore can exist for densities between the spinodals. For the open pores, the black contour lines indicate the gas phase pressure in kPa. Also, the bulk saturation pressure of 48.86 kPa is shown as a dashed white line. For all maps, unstable configurations are red, stable configurations are green and configurations that are locally stable, but have a larger energy than if the pore were filled with a single homogeneous phase, are orange.

to pore size) become unstable w.r.t. a homogeneous gas phase. A crucial difference from the free bubbles/droplets, however, is that the transition from stable to metastable depends on the contact angle.

The orange regions for the open pores indicate where the adsorbed/droplet bubble configurations are locally stable, but have a larger grand canonical energy than if the pore were filled with a homogeneous phase with the same intensive properties as the e-phase. The location of these regions does not change much when pore size is reduced, which is evident by comparing Figures 5b to 5d for the bubbles, and Figures 5a to 5c for the droplets.

Comparing the adsorbed bubbles in the large open pore (Figure 5b) with those in the small pore (Figure 5d), we observe that the variation of gas pressure is much larger in the small pores. In particular when the liquid phase is sufficiently wetting, the gas pressure is lower than the bulk saturation pressure, and much more so in the small pore. Although the external phase is liquid in Figure 5b and Figure 5d, these observation are closely related to the phenomenon of capillary condensation in open pores with an external gas phase. When the liquid phase is wetting, a lower water vapor pressure is required for water to condense in the pore than in the bulk. A much lower vapor pressure is required in the small pores, meaning that water will preferentially condense in small over large pores. A study of capillary condensation and the effects pore size and shape can be done with the models and methods presented here, which is a possible topic for future work.

4.3. Pore with a thick films of liquid or gas

The thermodynamic stability of liquid and gas films in open and closed pores is shown in Figure 6. Configurations are here mapped in terms of the position of the left contact line z_ℓ and contact angle.

In the open pores, most of the liquid (Figure 6a) and gas (Figure 6b) film configurations are unstable. The exception is when the film phase is strongly wetting. It is then possible to have a metastable film, which is evident by the orange regions in the left part of Figure 6a and the right part of Figure 6b. The stability map for the small pore in the open system is nearly identical to that of the large pore and is shown in the supplementary material.

Stability maps of liquid and gas films in the 10 μm closed pore are shown in Figure 6c and Figure 6d, respectively. They reveal large regions where both gas and liquid films are more stable than the homogeneous phase. In contrast to the adsorbed droplets, which appear when the liquid is non-wetting, the liquid films are stable only when the liquid is wetting. Analogously, the gas films in closed pores are locally stable only for a highly non-wetting liquid.

Figure 6 reveals that the thermodynamic stability of thick films is remarkably different in open and closed pores. A deeper insight into the origin of this difference can be gained by further investigating the unstable regions. Like the adsorbed bubbles and droplets discussed in Section 4.2, a translational instability is responsible for the unstable regions in the closed system, as can be seen in Figure 7a for the liquid film. This translation instability is also present in the same regions in the open pore (Figure 6a and Figure 6b). However, the open pore also has a condensation/evaporation instability which is present in the entire unstable region. This is illustrated in Figure 7b for the liquid film.

As for the previous two configuration types, a metastable region appears in the closed system when the pore size is reduced, as shown in Figure 6e and Figure 6f for the liquid and gas films, respectively. The metastable configurations represent films whose small gas and liquid volumes, again, do not compensate for their interfacial energy costs. In addition, an unstable region also appears for films with small extent along the z-axis. This region is present for both, but is larger for the gas film than the liquid film. It is caused by a condensation/evaporation instability.

We emphasize that the appearance of metastable regions and of condensation/evaporation instabilities cannot be predicted form a purely mechanical analysis of the film, and a complete thermodynamic stability analysis is needed. This is important critique to nearly all previous works that evaluate the stability of films in the literature, and an important future work is thus to extend the present analysis to films that have a non-zero disjoining pressure to shed new light on the thermodynamic stability of thin films in open and closed systems.

4.4. Phase diagrams

The final results we report are phase diagrams that show the equilibrium configuration, i.e. that which has the lowest total energy at given conditions. Such phase diagrams are shown in Figure 8 for closed pores of sizes 10 μm and 0.01 μm. The equilibrium configurations herein are determined by comparing the Helmholtz energies of the different (locally stable) fluid configurations at each value of ρ and α.

The phase diagram for the large pore in Figure 8a exhibits a large degree of symmetry around the neutral-wetting case where $\alpha = \pi/2$. As pore-size is reduced (Figure 8a), however, this symmetry is broken, partly due the appearance of homogeneous phases with lower Helmholtz energies than the heterogeneous structures. We note in particular the appearance of a stretched homogeneous liquid phase at the expense of the free bubble and adsorbed droplet configurations. In a similar manner, a compressed homogeneous gas phase appears as well.

For both phase diagrams, the free bubble and adsorbed droplet configurations prevail at higher densities, because locally stable configurations of these kinds allow for large liquid volume fractions. Similarly, the free droplet and adsorbed bubble are prevalent at lower densities, as these allow for large gas volume fractions. At densities around 25 mol l^{-1}, the equilibrium configuration is either a free bubble (when the liquid is wetting) or a free droplet (when the liquid is non-wetting).

Equilibrium liquid film configurations are only observed at low densities and for wetting liquids. In the 10 μm-pore, the extent of the liquid film region along the ρ-axis is smaller than the resolution used in the figure. A finer resolution of the low densities, however, reveals that the region is indeed there. Its

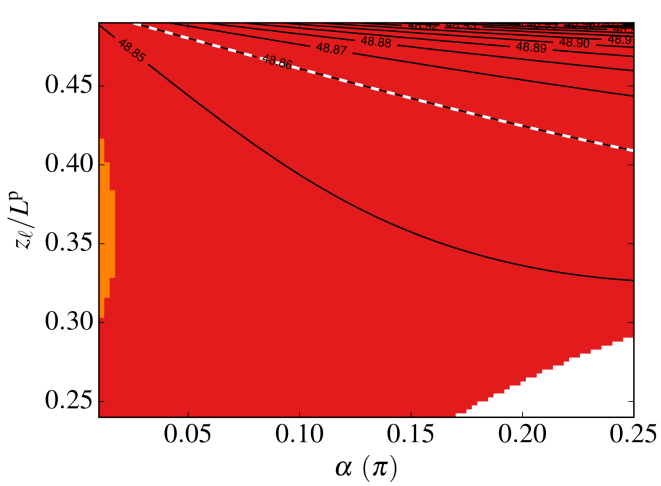

(a) Liquid films in open pore of 10 µm

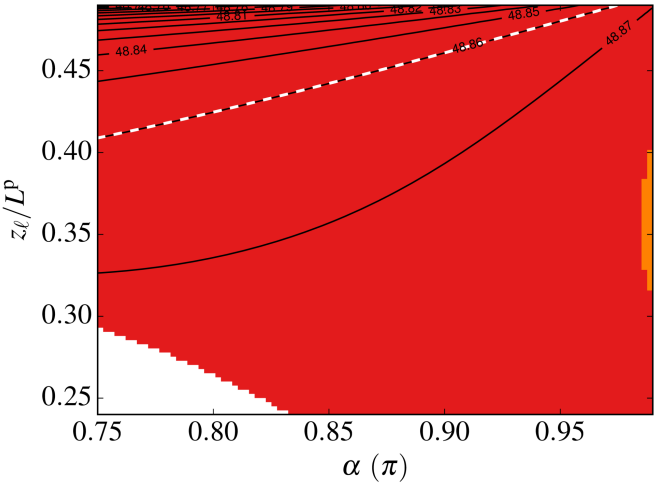

(b) Gas films in open pore of 10 µm

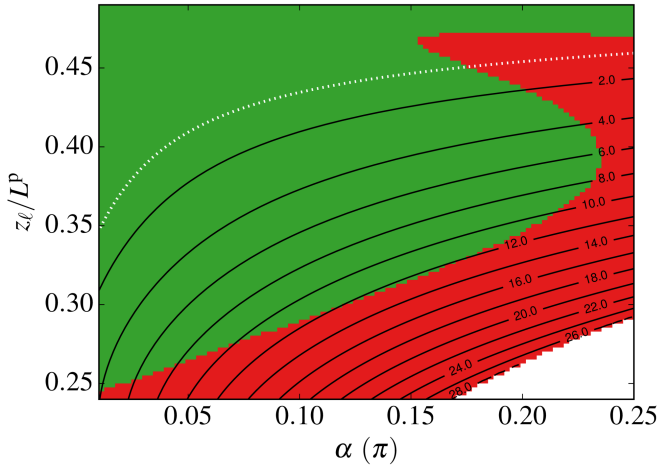

(c) Liquid films in closed pore of 10 µm

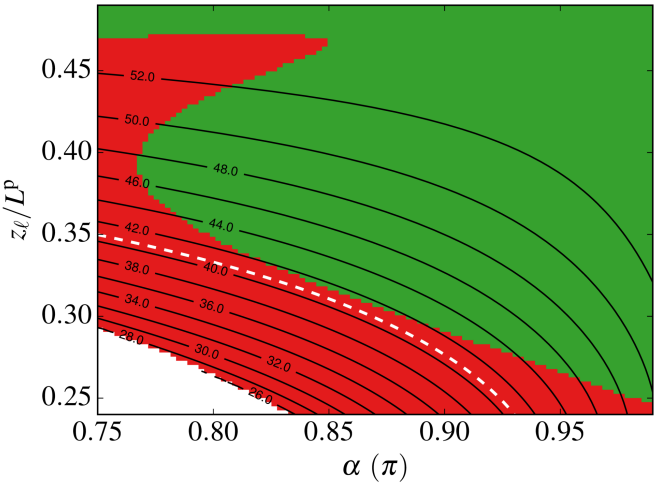

(d) Gas films in closed pore of 10 µm

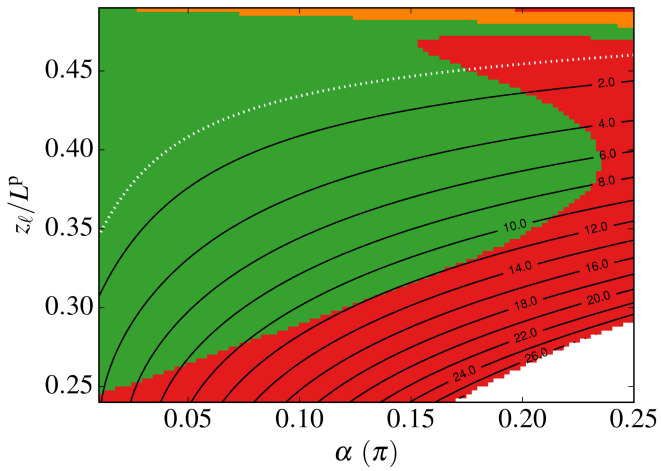

(e) Liquid films in closed pore of 0.01 µm

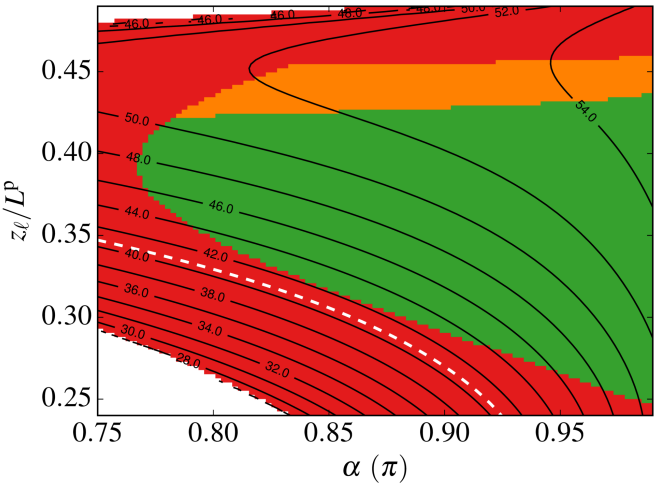

(f) Gas films in closed pore of 0.01 µm

Figure 6: Stability maps of (left column) liquid films and (right column) gas films in open and closed pores of lengths 10 µm and 0.01 µm. For the closed pores, the black contour lines indicate the total fluid density in mol l^{-1}. Further, the gas spinodal density of 1.05 mol l^{-1} is drawn as a dotted white line and the liquid spinodal of 40.7 mol l^{-1} is shown as a dashed white line. No homogeneous phase filling the entire pore can exist for densities between the spinodals. For the open pores, the black contour lines indicate the gas phase pressure in kPa. Further, the bulk saturation pressure of 48.86 kPa is shown as a dashed white line. In all maps, unstable configurations are red, stable configurations are green and configurations that are locally stable, but have a larger energy than if the pore were filled with a single phase, are orange.

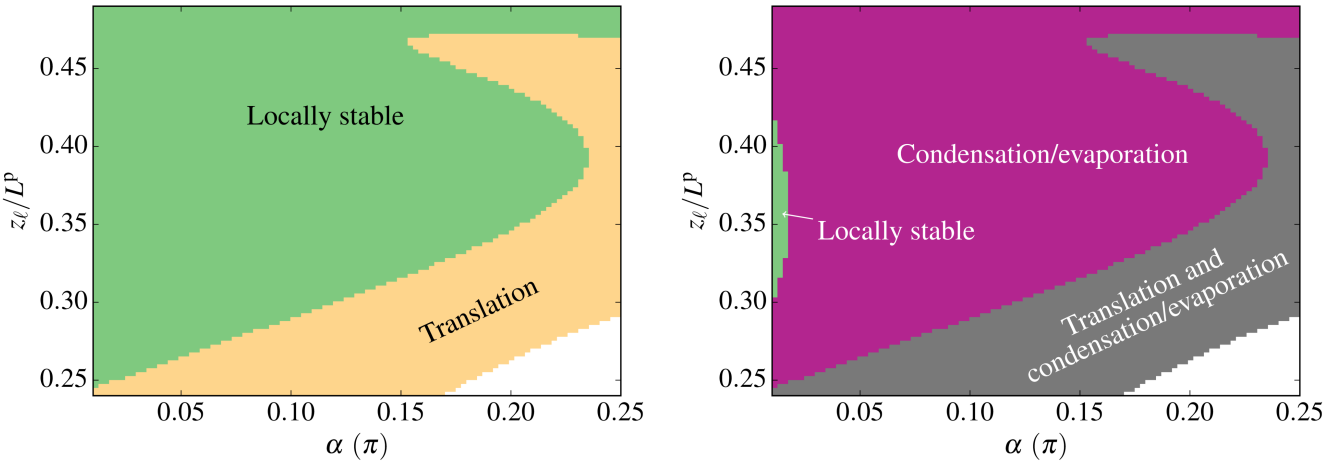

(a) (b)

Figure 7: Maps of instability types for liquid films in (a) the 10 µm closed pore and (b) the 10 µm open pore. Regions with no instabilities are light green, regions with only translation instabilities are cream, regions with only condensation/evaporation instabilities are purple and regions with both types of instabilities are gray.

position and extent along the α-axis is indicated by a thin solid line in Figure 8a.

The size of the liquid film region grows when the pore size is reduced (Figure 8b). This expansion is primarily at the expense of the adsorbed bubble region and can be explained as follows. When the pore size is reduced, the liquid pressures in the adsorbed bubble configurations are also reduced. Eventually, these pressures reach the liquid spinodal, where the liquid phase can no longer exist, and it is no longer possible to have an adsorbed bubble. This is also evident from comparing the white region in the lower left corner of Figure 5d with that in Figure 5b. The liquid film, however, is stable in this region as it has a lower curvature than the adsorbed bubble. It therefore appears in the phase diagram as the equilibrium configuration when it is no longer possible to have an adsorbed bubble.

Like the liquid film region in the 10 µm-pore (Figure 8a), the extent of the gas film region along the ρ-axis is smaller than the resolution. Its position is therefore also indicated with a thin solid line. The gas film appears at high densities, when the liquid is non-wetting. For the 10 nm-pore, however, we do not observe any gas films at equilibrium. The adsorbed droplet is found to always have a lower energy than the gas film. This conclusion may well change for other fluids and pore geometries.

For the closed pores at a given contact angle, a control parameter is the total density, i.e. how many particles the pore contains. For the open pores on the other hand, the particle reservoir connected to be pore is either gas or liquid and not both at the same time. We therefore present separate phase diagrams for cases where the external phase is gas (Figure 9) and cases when it is liquid (Figure 10). The equilibrium configurations are here determined by comparing the grand canonical energies of the different (locally stable) fluid configurations at each value of p^{e} and α.

For both pore sizes and external phase choices, a homogeneous phase is the prevailing fluid configuration. With an external gas phase, an adsorbed droplet appears as the liquid is non-wetting and, with an external liquid phase, an adsorbed bubble appears when the liquid is wetting. Compared to the phase diagrams for the closed pores, there are much fewer possible configurations. The free droplets and bubbles are absent because they are unstable for all possible contact angles and external pressures. The film configurations are absent because, even though they may be locally stable in an open pore, the homogeneous phase has a lower grand canonical energy.

As the pore size is decreased, the range of external pressures at which we find an adsorbed droplet or bubble is greatly increased. This is evident by comparing the scale of the ordinates of Figures 9 and 10. The increase in range is due to the increased Young–Laplace pressure difference of the interface induced by the large interfacial curvatures in the small pores.

5. Conclusion

We have studied the thermodynamic stability of free and adsorbed droplets, bubbles and gas and liquid films in open and closed pores by use of capillary models coupled to an equation of state. We used water at 358 K, as described by the SRK-CPA equation of state, as example. Emphasis was placed on the effect of fluid-solid interaction, as described by a finite contact angle, pore size and whether the pore is open or closed.

For free droplets and bubbles, our findings were in agreement with previous works [13, 16]. These configurations were unstable in open pores but could be stable in closed pores, if the bubbles/droplets were large enough.

In contrast to the free droplets and bubbles, adsorbed droplets and bubbles could be stable both in closed and open pores. Evidently, the interaction with the solid phase made these structures stable and in many cases, depending on contact angle and phase fractions, favorable w.r.t. a homogeneous fluid phase.

A new methodology was presented to analyze the thermodynamic stability of films, where the integral that describes the

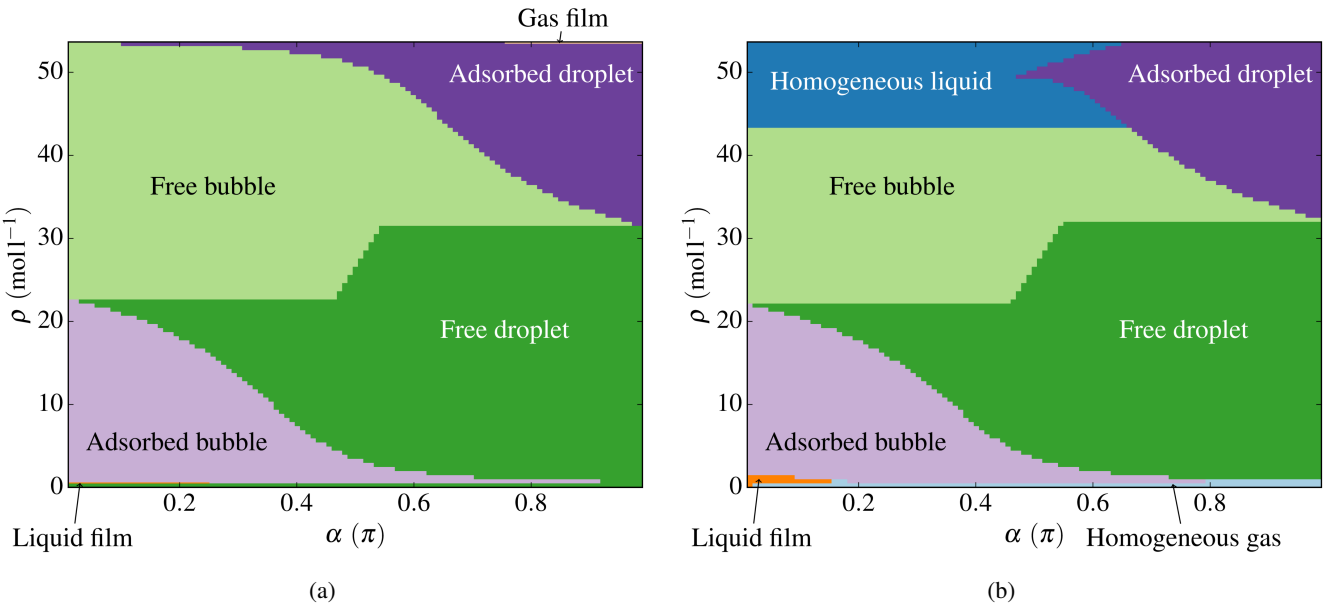

(a) (b)

Figure 8: Phase diagram showing equilibrium configurations in a closed pores of size (a) 10 µm and (b) 0.01 µm. Considered configurations are homogeneous gas (light blue), homogeneous liquid (blue), free bubble (light green), free droplet (green), adsorbed bubble (light purple), adsorbed droplet (purple), gas film (light orange) and liquid film (orange).

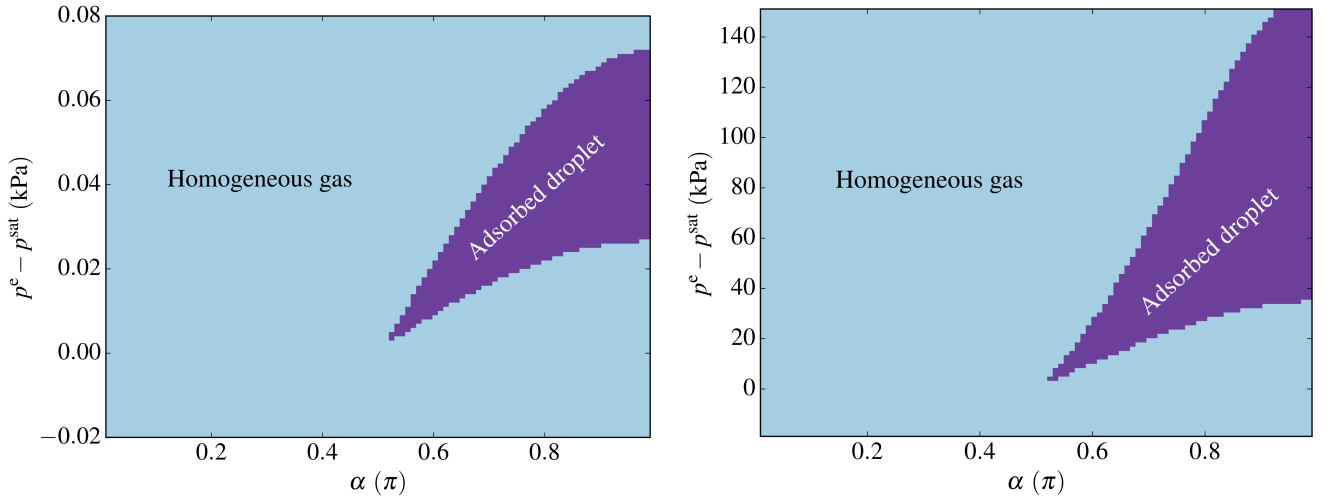

(a) (b)

Figure 9: Phase diagram showing equilibrium configurations in an open pore of size (a) 10 µm and (b) 0.01 µm and a gaseous external phase. Considered configurations are homogeneous gas (light blue) and adsorbed droplet (purple). External pressure minus the bulk saturation pressure, p^{sat} = 48.86 kPa, is indicated on the ordinate axis.

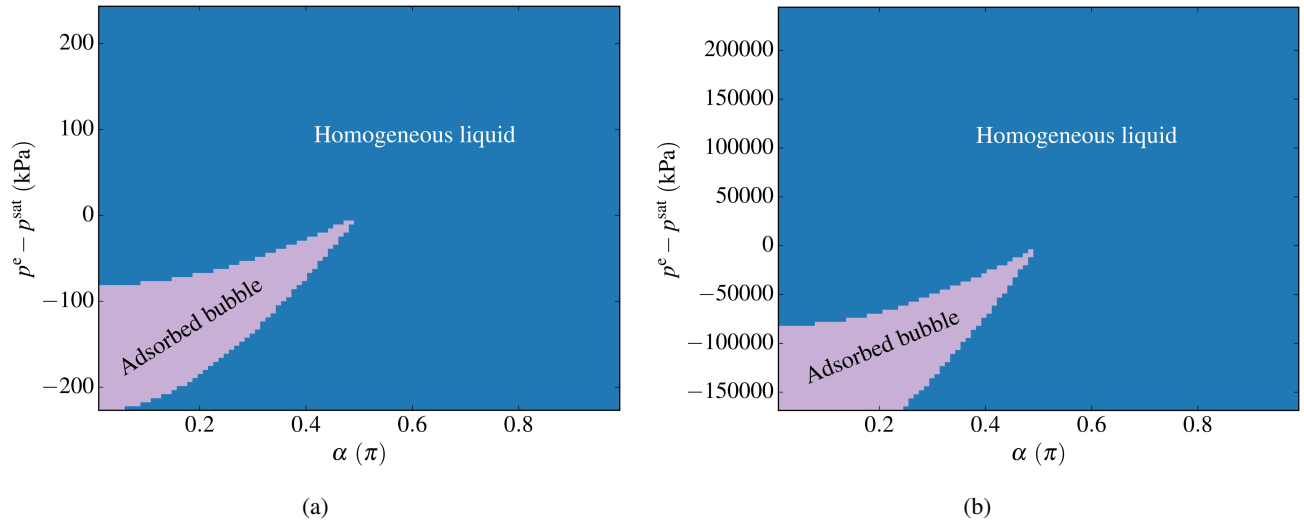

Figure 10: Phase diagram showing equilibrium configurations in an open pore of size (a) 10 µm and (b) 0.01 µm and a liquid external phase. Considered configurations are homogeneous liquid (blue) and adsorbed bubble (light purple). External pressure minus the bulk saturation pressure, $p^{sat} = 48.86$ kPa, is indicated on the ordinate axis.

total energy of the system was approximated by a quadrature rule. The methodology allowed us to examine in detail the perturbation that made the film unstable.

Gas and liquid films were found to be unstable at most conditions in the open pores. The exception was when the fluid was nearly perfectly wetting and a liquid film could form, or nearly perfectly non-wetting, when a gas film could form. In both cases, the films were metastable with respect to the homogeneous phase. In the closed pore, both stable gas and liquid films were found. As for the free droplets and bubbles, metastable regions where a homogeneous phase was energetically preferable were observed for both adsorbed droplets and bubbles and for the gas and liquid films in the small pore. The reason was that, as the volumes of the gas and liquid phases became smaller, the energy gained from having both a liquid and a gas phase did not compensate for the energy cost of the gas-liquid interface.

Observed instabilities for the adsorbed droplets/bubbles and the films belonged to one of two distinct classes: (1) translation and (2) condensation/evaporation. Although exceptions were present, the general trend was that translation instabilities were observed in the closed pores while both translation and condensation/evaporation instabilities were observed in the open pores.

Finally, we presented phase diagrams showing equilibrium configuration types for both open and closed pores. The closed-pore phase diagrams were found to contain a larger variety of structures compared to the open-pore diagrams. Partly, this is because the open-pore diagrams can contain only structures where the external phase is gas or liquid, while the closed-pore diagrams can have both kinds of structures. Most interesting, however, is the lack of locally stable configurations of free droplets/bubbles and films with lower energy than a homogeneous phase in the open pores.

The appearance of metastable regions and of condensation/evaporation instabilities cannot be predicted form a purely mechanical analysis of the systems. A complete thermodynamic stability analysis, as performed herein, is necessary. In previous literature on films, the discussion is usually limited to mechanical stability. The methodology presented in this work can be used to shed new light on the topic.

The analysis presented in this work is a step towards developing a thermodynamic framework to map the rich heterogeneous phase diagram of porous media and other confined systems.

Acknowledgments

This work was supported by the Research Council of Norway through its Centres of Excellence funding scheme, project number 262644.

Declaration of interest

Declarations of interest: none.

References

[1] T. Hiratsuka, H. Tanaka, and M. T. Miyahara. Comprehensive modeling of capillary condensation in open-ended nanopores: Equilibrium, metastability, and spinodal. *The Journal of Physical Chemistry C*, 121 (48):26877–26886, 2017. doi: 10.1021/acs.jpcc.7b09631.

[2] T. Horikawa, D. D. Do, and D. Nicholson. Capillary condensation of adsorbates in porous materials. *Advances in colloid and interface science*, 169(1):40–58, 2011. doi: 10.1016/j.cis.2011.08.003.

[3] A. V. Neimark and A. Vishnyakov. Gauge cell method for simulation studies of phase transitions in confined systems. *Physical Review E*, 62 (4):4611, 2000. doi: 10.1103/PhysRevE.62.4611.

[4] A. V. Neimark, P. I. Ravikovitch, and A. Vishnyakov. Inside the hysteresis loop: Multiplicity of internal states in confined fluids. *Physical Review E*, 65(3):031505, 2002. doi: 10.1103/PhysRevE.65.031505.

[5] F. Caupin, A. Arvengas, K. Davitt, M. E. M. Azouzi, K. I. Shmulovich, C. Ramboz, D. A. Sessoms, and A. D. Stroock. Exploring water and other liquids at negative pressure. *Journal of Physics: Condensed Matter*, 24 (28):284110, 2012. doi: 10.1088/0953-8984/24/28/284110.

[6] M. E. M. Azouzi, C. Ramboz, J.-F. Lenain, and F. Caupin. A coherent picture of water at extreme negative pressure. *Nature Physics*, 9(1):38, 2013. doi: 10.1038/nphys2475.

[7] Z.-Y. Wang and J. Wu. Ion association at discretely-charged dielectric interfaces: Giant charge inversion. *The Journal of Chemical Physics*, 147 (2):024703, 2017. doi: 10.1063/1.4986792.

[8] M. J. Blunt. Physically-based network modeling of multiphase flow in intermediate-wet porous media. *Journal of Petroleum Science and Engineering*, 20(3-4):117–125, 1998. doi: 10.1016/S0920-4105(98)00010-2.

[9] M. Kulmala, H. Vehkamäki, T. Petäjä, M. Dal Maso, A. Lauri, V.-M. Kerminen, W. Birmili, and P. McMurry. Formation and growth rates of ultrafine atmospheric particles: a review of observations. *Journal of Aerosol Science*, 35(2):143–176, 2004. doi: 10.1016/j.jaerosci.2003.10.003.

[10] J. A. Huberman and A. D. Riggs. On the mechanism of DNA replication in mammalian chromosomes. *Journal of Molecular Biology*, 32(2):327–341, 1968. doi: 10.1016/0022-2836(68)90013-2.

[11] H. B. Callen. *Thermodynamics and an introduction to thermostatistics*. John Wiley & Sons, New York, 1985.

[12] A. Fladerer and R. Strey. Homogeneous nucleation and droplet growth in supersaturated argon vapor: The cryogenic nucleation pulse chamber. *The Journal of Chemical Physics*, 124(16):164710, 2006. doi: 10.1063/1.2186327.

[13] Ø. Wilhelmsen, D. Bedeaux, S. Kjelstrup, and D. Reguera. Thermodynamic stability of nanosized multicomponent bubbles/droplets: The square gradient theory and the capillary approach. *The Journal of Chemical Physics*, 140(2):024704, 2014. doi: 10.1063/1.4860495.

[14] A. I. Rusanov. Surface thermodynamics revisited. *Surface Science Reports*, 58(5-8):111–239, 2005. doi: 10.1016/j.surfrep.2005.08.002.

[15] F. F. Abraham. *Homogenous nucleation theory: The pretransition theory of vapor condensation*. Academic Press, New York, 1974.

[16] A. J.-M. Yang. The thermodynamical stability of the heterogeneous system with a spherical interface. *The Journal of Chemical Physics*, 82(4): 2082–2085, 1985. doi: 10.1063/1.448344.

[17] P. Aursand, M. Aa. Gjennestad, E. Aursand, M. Hammer, and Ø. Wilhelmsen. The spinodal of single-and multi-component fluids and its role in the development of modern equations of state. *Fluid Phase Equilibria*, 436:98–112, 2017. doi: 10.1016/j.fluid.2016.12.018.

[18] Ø. Wilhelmsen, D. Bedeaux, S. Kjelstrup, and D. Reguera. Communication: Superstabilization of fluids in nanocontainer. *The Journal of Chemical Physics*, 141:071103, 2014. doi: 10.1063/1.4893701.

[19] Ø. Wilhelmsen and D. Reguera. Evaluation of finite-size effects in cavitation and droplet formation. *The Journal of Chemical Physics*, 142(6): 064703, 2015. doi: 10.1063/1.4907367.

[20] J. C. Berg. Fluid interfaces and capillarity. In *An introduction to interfaces and colloids – The bridge to nanoscience*, chapter 2. World Scientific, Singapore, 2009.

[21] L. Boinovich and A. Emelyanenko. Wetting and surface forces. *Advances in Colloid and Interface Science*, 165(2):60–69, 2011. doi: 10.1016/j.cis.2011.03.002.

[22] L. Boinovich and A. Emelyanenko. The prediction of wettability of curved surfaces on the basis of the isotherms of the disjoining pressure. *Colloids and Surfaces A: Physicochemical and Engineering Aspects*, 383 (1-3):10–16, 2011. doi: 10.1016/j.colsurfa.2010.12.020.

[23] A. V. Neimark. Thermodynamic equilibrium and stability of liquid films and droplets on fibers. *Journal of Adhesion Science and Technology*, 13 (10):1137–1154, 1999. doi: 10.1163/156856199X00839.

[24] A. V. Neimark and K. G. Kornev. Classification of equilibrium configurations of wetting films on planar substrates. *Langmuir*, 16(13):5526–5529, 2000. doi: 10.1021/la000267b.

[25] D. Bhatt, J. Newman, and C. Radke. Molecular simulation of disjoining-pressure isotherms for free liquid, Lennard–Jones thin films. *The Journal of Physical Chemistry B*, 106(25):6529–6537, 2002. doi: 10.1021/jp0202136.

[26] H. Hu and Y. Sun. Molecular dynamics simulations of disjoining pressure effect in ultra-thin water film on a metal surface. *Applied Physics Letters*, 103(26):263110, 2013. doi: 10.1063/1.4858469.

[27] A. Nold, D. N. Sibley, B. D. Goddard, and S. Kalliadasis. Fluid structure in the immediate vicinity of an equilibrium three-phase contact line and assessment of disjoining pressure models using density functional theory. *Physics of Fluids*, 26(7):072001, 2014. doi: 10.1063/1.4886128.

[28] A. Checco, B. M. Ocko, M. Tasinkevych, and S. Dietrich. Stability of thin wetting films on chemically nanostructured surfaces. *Physical review letters*, 109(16):166101, 2012. doi: 10.1103/PhysRevLett.109.166101.

[29] J. L. Troutman. *Variational calculus and optimal control*. Springer, second edition, 1996.

[30] Ø. Wilhelmsen, G. Skaugen, M. Hammer, P. E. Wahl, and J. C. Morud. Time efficient solution of phase equilibria in dynamic and distributed systems with differential algebraic equation solvers. *Industrial & Engineering Chemistry Research*, 52(5):2130–2140, 2013. doi: 10.1021/ie302579w.

[31] A. Aasen, M. Hammer, G. Skaugen, J. P. Jakobsen, and Ø. Wilhelmsen. Thermodynamic models to accurately describe the $PVTxy$-behavior of water/carbon dioxide mixtures. *Fluid Phase Equilibria*, 442:125–139, 2017. doi: 10.1016/j.fluid.2017.02.006.

[32] M. L. Michelsen and J. M. Mollerup. *Thermodynamic Models: Fundamentals & Computational Aspects*. Tie-Line Publications, Holte, second edition, 2007.

[33] Ø. Wilhelmsen, A. Aasen, G. Skaugen, P. Aursand, A. Austegard, E. Aursand, M. Aa. Gjennestad, H. Lund, G. Linga, and M. Hammer. Thermodynamic modeling with equations of state: present challenges with established methods. *Industrial & Engineering Chemistry Research*, 56(13): 3503–3515, 2017. doi: 10.1021/acs.iecr.7b00317.

[34] E. Jones, T. Oliphant, P. Peterson, et al. SciPy: Open source scientific tools for Python, 2001–. URL `http://www.scipy.org/`.

[35] P. Linstrom and W. Mallard, editors. *NIST Chemistry WebBook, NIST Standard Reference Database Number 69*. National Institute of Standards and Technology, Gaithersburg MD, 20899. doi: 10.18434/T4D303.

[36] E. Anderson, Z. Bai, C. Bischof, S. Blackford, J. Demmel, J. Dongarra, J. Du Croz, A. Greenbaum, S. Hammarling, A. McKenney, and D. Sorensen. *LAPACK Users' Guide*. Society for Industrial and Applied Mathematics, Philadelphia, PA, third edition, 1999. ISBN 0-89871-447-8.

[37] T. Bednarek and G. Tsotridis. Issues associated with modelling of proton exchange membrane fuel cell by computational fluid dynamics. *Journal of Power Sources*, 343:550–563, 2017. doi: 10.1016/j.jpowsour.2017.01.059.

Appendix A. Solutions to the film Euler–Lagrange equation

A complicating factor in the search for stationary states for the film is that there may be many solutions to $\mathbf{G} = \mathbf{0}$ with a specified z_ℓ. $\mathbf{G}$ is the residual function for the two-point boundary value problem obtained by setting (46) equal to $\mathbf{0}$. One example is illustrated in Figure A.11, which displays a pore with $L^\mathrm{p} = 10\,\mu\mathrm{m}$, where the shape of the pore is defined by (1) and drawn in black in Figure A.11b. Furthermore, the contact angle is $\alpha^\mathrm{n} = 0.07\pi$, $\sigma^\mathrm{en} = 0.0616\,\mathrm{N\,m^{-1}}$ and $z_\ell = 3\,\mu\mathrm{m}$. Figure A.11a maps the search space. The dotted curve shows where the first element of $\mathbf{G}$ is zero and the boundary condition on R^f is satisfied, while the dashed curve shows where the second element of $\mathbf{G}$ is zero and the boundary condition on $\dot{R}^\mathrm{f}$ is satisfied. A solution to the two-point boundary value problem is thus a point where the two curves intersect. The solid vertical line is drawn at $z_\mathrm{r} = L^\mathrm{p} - z_\ell$. Solutions falling on this line are symmetric or anti-symmetric with respect to the center of the pore.

Four different solutions are indicated by circles (blue, green, red and yellow) in Figure A.11a. The corresponding film configurations are shown in Figure A.11b. Of these four solutions, only the green and the yellow are symmetric. When evaluating the thermodynamic stability of these solutions, however, it turns out that only the green solution is stable in a closed system. All solutions are unstable in an open system. For a more thorough discussion on thermodynamic stability, we refer to Section 4.

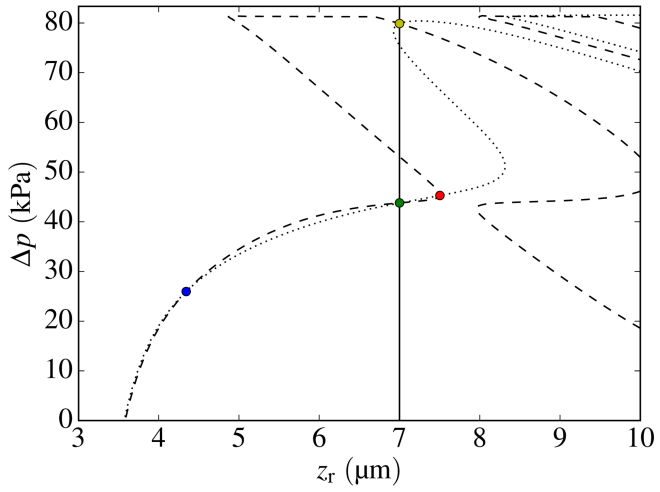

(a)

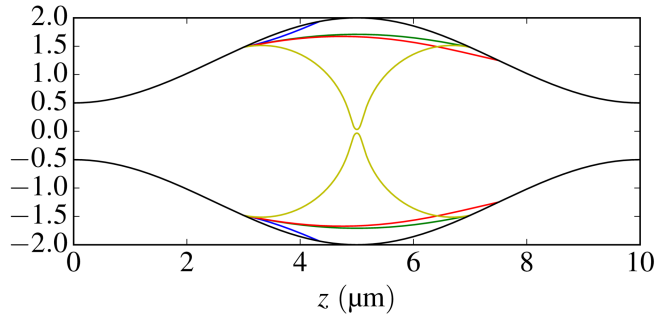

(b)

Figure A.11: Illustration of different solutions to the film ODE (39) for a given pore, shown in (b), $z_\ell = 3\,\mu\text{m}$ and $\alpha^n = 0.07\pi$. A map of the space searched for solutions to the two-point boundary value problem $\mathbf{G} = \mathbf{0}$ is shown in (a). The dotted curve indicates where the first element of $\mathbf{G}$ is zero and the boundary condition on R^f is satisfied. The dashed curve indicates where the second element of $\mathbf{G}$ is zero and the boundary condition on $\dot{R}^f$ is satisfied. A solution to the two-point boundary value problem is thus a point where the two curves intersect. Four different solutions are indicated (blue, green, red and yellow). The corresponding film profiles are shown in (b).

Since we observe that solutions that are not symmetric around the pore center are always unstable, we only need to consider the symmetric film solution with the lowest Δp, that is also feasible in the sense that $0 < R^f(z) < R^p(z)\,\forall z \in (z_\ell, z_r)$. In the analysis presented in this paper, we ignore the other solutions, even if they also represent unstable stationary states of the film. These unstable states may, however, be of interest in the theory of nucleation. For instance, the yellow profile in Figure A.11b could well be the saddle point that determines the activation barrier to the creation of a an adsorbed droplet, similar to the one depicted in Figure 1c.

Appendix B. Convergence of the discrete film description method

In Section 3.3, we presented a discrete method to describe the Helmholtz energy of the film. Here, we perform a convergence study to show that the solutions provided by the discrete method converge to those obtained by solving the Euler–Lagrange equations when the discrete grid is refined. To this end, we consider a pore described by (1) with $L^p = 10\,\mu\text{m}$ and choose $\alpha^n = \pi/20$ and $\sigma^{en} = 0.02\,\text{N m}^{-1}$. The fluid is, as in Section 4, water at 358 K, described by the CPA-SRK EOS. The film is liquid and the surrounding phase gas.

We use the variational formulation to obtain a stationary state of F where the film starts at $z_\ell = 0.3L^p$. This solution will serve both as a reference solution and to generate initial guesses for the discrete solutions. Subsequently, we solve (63) for different number of grid points, M. Relative errors in the film profile $\mathbf{R}^f$ with respect to the reference solution, as measured in the L_2- and L_∞-norms, and the corresponding estimated convergence orders are presented in Table B.1. It is clear from these results that the discrete solutions converge to the variational solution as the grid is refined, and that the convergence is second-order.

Table B.1: Relative errors in the film profile $\mathbf{R}^f$ with respect to the reference solution, as measured in the L_2- and L_∞-norms, for different discrete grid sizes M. The corresponding estimated convergence orders are also given.

M	L_2-error	L_2-order	L_∞-error	L_∞-order
25	$5.10 \cdot 10^{-5}$	-	$8.58 \cdot 10^{-4}$	-
50	$6.91 \cdot 10^{-6}$	2.88	$1.99 \cdot 10^{-4}$	2.11
100	$1.00 \cdot 10^{-6}$	2.79	$4.74 \cdot 10^{-5}$	2.07
200	$1.56 \cdot 10^{-7}$	2.69	$1.15 \cdot 10^{-5}$	2.04
400	$2.55 \cdot 10^{-8}$	2.61	$2.84 \cdot 10^{-6}$	2.02